KARADENİZ TECHNICAL UNIVERSITY
THE GRADUATE SCHOOL OF NATURAL AND APPLIED SCIENCES

PHYSICS DEPARTMENT

DEVELOPMENT OF SIMULATION CODES FOR SPECT AND PET IMAGING SYSTEMS

DOCTORAL THESIS

ANES MOHAMMED SALIH QASIM HAYDER

AUGUST 2025
TRABZON

KARADENİZ TECHNICAL UNIVERSITY

THE GRADUATE SCHOOL OF NATURAL AND APPLIED SCIENCES

PHYSICS DEPARTMENT

DEVELOPMENT OF SIMULATION CODES FOR SPECT AND PET IMAGING SYSTEMS

ANES MOHAMMED SALIH QASIM HAYDER

This thesis is accepted to give the degree of

DOCTOR OF PHILOSOPHY

By

The Graduate School of Natural and Applied Sciences at

Karadeniz Technical University

The Date of Submission : 29 / 07 /2025

The Date of Examination : 20 / 08 /2025

Thesis Supervisor : Tuncay BAYRAM

Trabzon 2025

PREFACE

This study, titled “Development of Simulation Codes for SPECT and PET Imaging Systems”, was prepared as part of the requirements for a PhD degree at the Graduate School of Natural and Applied Sciences, Karadeniz Technical University, Department of Physics.

First and foremost, I would like to express my sincere gratitude to my supervisor, Prof. Dr. Tuncay Bayram, for his continuous support, insightful guidance, and encouragement throughout the course of this study. His expertise and mentorship were instrumental in shaping the direction and quality of this work.

I would also like to extend my appreciation to all the members of the Nuclear Physics and Applications (NUCPAP) research group.

I would like to thank Prof. Dr. Bircan SÖNMEZ for her valuable support and for providing me with the facilities to work on the PET scan.

I sincerely thank my family for their endless support. A special thanks to my dear wife for her love, patience, and encouragement throughout this journey.

Anes HAYDER

Trabzon 2025

THESIS STATEMENT

I here by declare that I have completed this study, titled “Development Of Simulation Codes For SPECT And PET Imaging Systems,” submitted as my PhD dissertation, under the supervision of my advisor, Prof. Dr. Tuncay BAYRAM, from start to finish. I confirm that I independently collected the data/samples, conducted the experiments/analyses in the relevant Hospital, and have fully cited and referenced information obtained from other sources within the text and bibliography. I also declare that I have adhered to scientific research and ethical principles throughout the study and accept all legal consequences should any violations be revealed. 20/08/2025

Anes HAYDER

CONTENTS

Page No

PhD. Thesis

SUMMARY

DEVELOPMENT OF SIMULATION CODES FOR SPECT AND PET IMAGING SYSTEMS

Anes HAYDER

Karadeniz Technical University
The Graduate School of Natural and Applied Sciences
Department of Physics
Supervisor: Prof. Dr. Tuncay BAYRAM
2025, 91 Pages

Single photon emission tomography (SPECT) and positron emission tomography (PET) technologies are widely utilized for diagnosis in nuclear medicine. These imaging devices provide knowledge at the physiological, metabolic, and molecular levels. The image quality that is obtained via both SPECT and PET scanners is impacted by the geometric design and physical properties of component materials. Today, simulation platforms are indispensable tools for the optimization and modification of devices in the field of nuclear medicine. Simulation methods are not only cost- and time-effective in design but are also used as effective tools in the development of new imaging systems. In this context, the subject of this thesis is to develop simulation codes for the dual-head Mediso Any Scan S SPECT at SBU Trabzon Kanuni Training and Research Hospital and the GENERAL ELECTRIC (GE) Discovery-IQ PET model positron emission tomography (PET) imaging systems at KTU Farabi Hospital International In this context, GEANT4-based simulation codes were developed for the relevant SPECT and PET systems. The validity of these codes was verified by comparing them with experimental performance parameters for both SPECT and PET systems. Furthermore, collimator optimization was performed in addition to intrinsic performance parameters for the modelled SPECT scanner using various scintillation crystals.

Key Words: SPECT, PET, MonteCarlo, Simulation, GATE, Optimization.

Doktora Tezi

ÖZET

SPECT VE PET GÖRÜNTÜLEME SİSTEMLERİ İÇİN BENZETİM GELİŞTİRME

Anes HAYDER

Karadeniz Teknik Üniversitesi
Fen Bilimleri Enstitüsü
Fizik Anabilim Dalı
Danışman: Prof. Dr. Tuncay BAYRAM
2025, 91 Sayfa

Tek foton emisyon tomografisi (SPECT) ve pozitron emisyon tomografisi (PET) teknolojileri nükleer tıpta tanı amacıyla yaygın olarak kullanılmaktadır. Bu görüntüleme cihazları fizyolojik, metabolik ve moleküler düzeylerde bilgi sağlar. Hem SPECT hem de PET tarayıcıları ile elde edilen görüntü kalitesi, bileşen malzemelerin geometrik tasarımı ve fiziksel özelliklerinden etkilenir. Günümüzde simülasyon platformları, nükleer tıp alanında cihazların optimizasyonu ve modifikasyonu için kullanılan vazgeçilmez araçlardır. Simülasyon yöntemleri, sadece tasarımlarda maliyet ve zaman açısından etkili olmayıp aynı zamanda yeni görüntüleme sistemlerinin geliştirilmesinde de etkili araçlar olarak kullanılmaktadır. Bu bağlamda bu tez çalışması konusu, SBÜ Trabzon Kanuni Eğitim ve Araştırma Hastanesi'ndeki çift başlı Mediso Any Scan S SPECT ve KTÜ Farabi Hastanesi 'ndeki GENERAL ELECTRIC (GE) Discovery-IQ PET model pozitron emisyon tomografisi (PET) görüntüleme sistemleri için simülasyon kodları geliştirmektir. Bu çerçevede ilgili SPECT ve PET sistemleri için GEANT4 tabanlı simülasyon kodları geliştirilmiştir. Geliştirlen bu kodların geçerliliği hem SPECT ve hem de PET sistemlerinin deneysel performans parametreleri ile karşılaştırılarak doğrulanmıştır. Ayrıca, modellenen SPECT tarayıcısı için çeşitli sintilasyon kristalleri kullanılarak, içsel performans parametrelerine ek olarak kolimatör optimizasyonu da gerçekleştirilmiştir.

Anahtar Kelimeler: SPECT, PET, MonteCarlo Simülasyonu, GATE, Optimizasyon.

FIGURES

Page No

TABLES

Page No

LIST OF SYMBOLS

$BR_{\beta+}$: Ratio for positron emission

µ : Standard Deviation

σ : Sigma

AAPM : American Association of Physicists in Medicine

ACD : Analog-to-digital conversion

CFOV : Center field of view

CsI(TI) : Thallium-doped cesium iodide

CT : Computed Tomography

DU : Differential intrinsic uniformity

EANM : European Association of Nuclear Medicine

FOV : Field of view

FWHM : Full width half maximum

GAGG : Gadolinium Aluminum Gallium Garnet

GEANT4 : Geometry and Tracking

HEGP : High-energy general purpose

IAEA : International Atomic Energy Agency

IU : Integral uniformity

$LaBr_3$: Lanthanum Bromide

$LaCI_3$: Lanthanum Chloride

LSF : Line spread function

LEHR : Low-energy high resolution

LEGP : Low-energy general purpose

MC : Monte Carlo

MTF : Modulation Transfer Function

NaI(TI) : Thallium-doped sodium iodide

NEMA :National Electrical Manufacturers Association

NECR : Noise Equivalent Count Rate

PET : Positron Emission Tomography

QC : Quality control Test

PMT : Photomultiplier tube

ROI **:** Region of interested

SPECT **:** Single Photon Emission Tomography

UFOV **:** Useful field of view

$YAlO_3$ **:** Yttrium Aluminium Perovsk

1. GENERAL INFORMATION

1.1. General Overview

Nuclear imaging is a crucial branch of nuclear medicine that focuses on clinical diagnostics. It visualizes and assesses physiological activities (metabolic, molecular, and functional information) within the human body. SPECT and PET are essential imaging modalities used in this field (Payolla et al., 2019). These modalities rely on the detection of gamma radiation emitted by the administered radiopharmaceuticals injected into the human body to create a map of the radiation coming from the area being imaged (Hacker et al., 2015). These imaging instruments could be applied in various areas, such as cardiovascular, neurological, oncological, immunological, and pharmaceutical research (Famjm & Mjg, 2012). In addition, combining anatomical imaging techniques CT, with functional techniques, such as "SPECT" and "PET", results in more accurate diagnoses, which eventually aid in designing personalized treatment protocols (Bailey et al., 2014; Gündoğdu et al., 2018).

Usually the SPECT consists of dual heads; each head is composed of three main components, which are collimator, crystal, and photomultiplier (PMT). In contrast, the blocks of pixilated scintillation crystals arranged in an array of rings constitute the PET detector (Fleck et al., 2021; Grupen & Buvat, 2011; Kharfi, 2013). The operating mechanism of the SPECT device is categorized into four stages. Collimators filter and direct the emitted gamma radiation at the first stage before it hits the crystal (Sharp et al, 2005). The filtered gamma radiation interacts with SPECT's scintillation crystal and transforms it into visible light at this stage. In the third stage, the PMT and electronics convert the visible light into digital signals (Dahlbom, 2017). Finally, the digital signals are reconstructed by the reconstruction application using one of the reconstruction methods to generate a 2-dimensional image of the distributed gamma radiation (Kharfi, 2013). While the SPECT imaging device utilizes different kinds of collimators based on the imaging application to guide gamma radiation, the PET imaging device detects the two opposite gamma radiations with 511 keV energy and a 180-degree angle (coincidence) that are emitted by the positron annihilation. Afterwards, the detected gamma radiation goes through the aforementioned stages of the SPECT imaging device to create a 3-dimensional image.

The radionuclides (^{99m}Tc, ^{111}In, ^{123}I, ^{131}I, ^{67}Ga, etc.) used in SPECT imaging generally emit γ-rays with energies in the range of ~70 to 400 keV and have longer half-lives than the rapidly decaying positron-emitting radionuclides (^{11}C, ^{13}N, ^{18}O, ^{68}Ga, ^{18}F, etc.) used in PET (Crișan, 2022). Furthermore, the positron-emitting radionuclides should be characterized by a high branching ratio for positron emission ($BR_{\beta+}$), minimal or negligible gamma ray emissions, limited positron energy to ensure optimal spatial resolution, and suitable chemical properties. Some of these features for medical radionuclides directly determine the material's physical properties and geometric parameters of collimators and scintillation crystals (Conti, 2016; Alauddin, 2011).

Long-term use of the gamma camera causes damage to or consumption of the device's main parts. This consumption leads to a change in performance parameters from the values it was manufactured with and, thus, a change in the device's performance (Soni, 1992). These alterations manifest as deformities in the image. Performance evaluations are conducted to ensure the equipment functions correctly. The evaluations conducted before the clinical use of gamma cameras are referred to as an acceptance quality control test (QC). The purpose of these tests is to confirm that a particular gamma camera meets the technical and performance specifications provided by the manufacturer (Nuzzo, 2019). On the other hand, there are regular quality control tests implemented daily, monthly, and annually; these tests are called routine tests. Generally, the QC of gamma cameras includes physical inspection, spatial resolution, uniformity, linearity, energy resolution, count rate response, sensitivity, and pixel size (MacManus et al., 2009). These quality control tests for the SPECT imaging device are categorized as intrinsic and extrinsic. Intrinsic performance parameters are conducted without collimators and reflect the performance of the SPECT imaging device's crystal and electronics. Whereas the system performance parameters of the SPECT imaging device, which refer to extrinsic parameters, are performed with collimators. The general system QC of the PET imaging device includes sensitivity, spatial resolution, energy resolution, and count rate performance (Saha, 2012; Zanzonico, 2014). The quality tests are identified by a couple of organizations, such as the International Atomic Energy Agency (IAEA), the American Association of Physicists in Medicine (AAPM), the European Association of Nuclear Medicine (EANM), and National Electrical Manufacturers Association (NEMA).

Generally, several parameters influence the performance of nuclear imaging devices (SPECT and PET), including geometrical configuration and dimensions, the material type of these devices' components (crystals and collimators), and the electronic characteristics used to amplify and analyse the visible light (Moslemi & Ashoor, 2017). Extrinsic performance characteristics are associated with some of these factors, whereas intrinsic performance parameters are associated with others (Fuin et al., 2010).

The extrinsic performance parameters of the SPECT device are significantly influenced by the geometric dimensions of the collimator (Asmi et al., 2020). The sensitivity and spatial resolution are directly affected by the hole diameter and collimator thickness, which is defined as the hole length. The system sensitivity improves with an increased diameter and a reduced hole length. Conversely, the system's spatial resolution degraded (Abbaspour et al., 2018). Consequently, it affects the trade-off (balance) between system sensitivity and spatial resolution. As well as these characteristics of collimators directly influence the image contrast by rejecting the septa-penetrating events and the scattering events (Rong & Frey, 2013; Fenghua et al., 2016).

Intrinsic performance parameters are significantly impacted by the crystal's physical properties. These include density, effective atomic number, decay time, and light yield, as well as its thickness, which affects intrinsic spatial resolution (Prekeges, 2013; Xu, Yan, & Wei, 2024). Typically, crystals that possess higher atomic numbers exhibit greater stopping power, hence augmenting sensitivity. In contrast, increased highlight yields improve the signal-to-noise ratio and energy resolution (Bergmann et al., 2009).

Simulations are an important artificial method utilized for testing and optimizing novel strategies in real scientific experiments and physical phenomena in many scientific research fields (Arce et al., 2021). Due to the complexity of physics in real experiments, where controlling the effects of underlying physical phenomena can be challenging, simulations serve as a valuable tool for investigating the impact of individual physical phenomena or specific parameters (Holstensson et al., 2010). Especially in the fields of nuclear physics and particle physics, the Monte Carlo (MC) simulation methods are extensively utilized. It provides precise values that agree with actual experimental results of nuclear interactions (Sarrut et al., 2021). In addition, simulation allows easy analysis instead of direct, costly, and time-consuming experiments (Li et al., 2015). The Monte Carlo applications that are employed to simulate nuclear instruments are SIMIND, EGS, MCNP, FLUKA, Open GATE, Penelope, and GEANT4. In the nuclear imaging field, the imaging devices' performance is enhanced via optimizing and modifying the SPECT and PET components using MC platforms on a large scale. GATE is one of the GEANT4 platforms specially designed for the simulation of nuclear imaging and radiotherapy devices, for example, SPECT, PET, and CT. This platform has unique features, such as supporting dynamic imaging and time-dependent source modeling, which leads to the simulation of physiological processes (patient movements) as well as radioactive source half-lives (Massari et al., 2020; Winterhalter et al., 2020). These features made it dominant in the nuclear imaging field. In this context, some studies performed with the GATE simulation code, which is used effectively for SPECT and PET, are listed below.

1.2. Literature Review

The validation of the GATE code was investigated by simulating the CsI(Na) pixel gamma camera used in the dual-headed animal SPECT system at Tehran University of Medical Sciences. In this study, the imaging quality control parameters (energy spectrum resolution, spatial resolution, and absolute sensitivity) measured by simulation and experimentally were compared. The obtained values from this comparison were ~13% and ~18% for the energy spectrum resolution, 2.4 and 2.5 mm for the spatial resolution, and 1.35 and 1.31 cps/μCi for the absolute sensitivity (Taherparvar & Sadremomtaz, 2018). K. Assié and his team conducted a study on the validation of GATE using an Indium-111 radioactive source. In the study, the researchers compared the simulated values of spatial resolution and sensitivity with the experimental measurements. As a result of this study, the differences between the simulation and experimental values were under 2% for spatial resolution and under 4% for sensitivity values when the distance from the source to the collimator ranged from 0 to 20 cm (K Assié et al., 2005). In a study conducted by Sadremomtaz & Telikani (2018), imaging protocols for the small animal SPECT system were compared using three independent Monte Carlo codes (SIMIND, MCNP-X, and GATE). The energy resolutions obtained from simulations using SIMIND, MCNP-X, and GATE were 17.53%, 19.24%, and 18.26%, respectively, while the experimental result was 19.15%. The spatial resolutions simulated by SIMIND, MCNP-X, and GATE were 3.18 mm, 2.90 mm, and 2.62 mm, respectively, while the experimental test reported this parameter as 2.82 mm. The sensitivity values obtained from simulations using SIMIND, MCNP-X, and GATE, as well as experimental tests, were 1.44, 1.27, 1.38, and 1.32 cps/μCi, respectively. In 2023, research conducted by Strugari et al. (2023) validated the GATE platform to mimic the Cubresa Spark SiPM-based preclinical SPECT scanner using the NEMA NU 1-2018 (NEMA, 2018) quality control standard. This research examined many intrinsic and extrinsic performance characteristics of the SPECT imaging device, including spatial resolution, linearity, uniformity, count rate, energy resolution, system resolution, and planar sensitivity. As a consequence, all simulated intrinsic and extrinsic performance parameters matched with measured data, with the most significant differences found below 7%.

A study conducted by Wang et al. (2023) employed the GATE platform in a new cardiac SPECT configuration. In this work, a collimator-less cardiac SPECT system is composed of seven mosaic patterns; each pattern consists of 10 cylinder blocks with many small, individual, separated scintillator pieces or tiles (1.68 mm × 1.68 mm × 20 mm) arranged together to form a larger detector surface. In contrast, a lab-designed prototype imaging system was created to demonstrate the feasibility of performing collimator-less SPECT imaging instead of validating the predicted performance in simulations. A lab prototype comprised a singular mosaic-patterned GAGG(Ce) detector block (2.1 mm × 2.1 mm × 20.0 mm, with a 4.2 mm separation between adjacent scintillator bars) measuring 67.5 mm × 67.5 mm × 20 mm, which was mechanically rotated through 13 positions to mimic a partial ring system. Utilizing separate multi-point sources for the lab prototype and hot-rod, disk, and 3D anthropomorphic cardiac phantoms for the simulated model, the performance of these systems was evaluated. Results showed sensitivity is 16.31%, and the 6-mm rods in the hot rod phantom and the 5-mm disks in the disk phantom are separable in simulated cardiac SPECT. The lab-prototype system were found to be capable of separating point sources with an 8 mm center-to-center distance in different positions across the field of view (FOV).

In this regard, the optimization and design of novel geometrical shapes of the different collimator types, digitizer modeling, and investigation of the influences of the crystal's dead layer and pixel size on the SPECT performance have been investigated using the GATE simulation platform in many studies (Beijst et al., 2015; Rasouli et al., 2010; Rault et al., 2011; Uslu et al., 2025).

Regarding the usage of GATE for PET, Rezaei et al., (2023) studied the capability of the GATE to validate the uEXPLORER PET device. In this work, the modeling of phantoms utilized for performance parameter tests, like spatial resolution, sensitivity, and count rate, relies on NEMA-NU2 2018 standards. Simulation and experimental measurement outcome differences for sensitivity, NECR, and FWHM were 2.3%, 9.9%, and 0.12 mm, respectively. In other works done by (Schmidtlein et al., 2006; Sheen et al., 2015; Sheikhzadeh et al., 2017), the same parameters were evaluated to investigate the GATE validation for modelling the GE Discovery 600 scanner, NeuroPET scanner, and GE Advance/Discovery LS PET scanner. The results obtained by simulated PET scanner models agree with experimental values of FWHM, sensitivity, and NECR within 2%-2.5%, 2.7%-5%, and 5.5%-18%, respectively.

The effect of the coincidence window and dead time on the count rate's performance employing the GATE platform was investigated by Saaidi et al. (2018). Throughout this research, the performance parameters of the ECAT EXACT HR PET scanner were validated according to NEMA NU 2-2012 standard, and the simulated data show excellent agreement with experimental data. The results of this investigation demonstrated a 28% decrease in Noise Equivalent Count Rate (NECR) value with coincidence time decreasing. Additionally, the NECR experiences an increase of 4.28% when utilizing 4900 ns non-paralyzable deadtime compared to 5000 ns paralyzable deadtime. In a comparative investigation done by Abi-Akl et al, (2023), the performance parameters for the two simulated PET scanners with different axial fields of view were compared. The monolithic LYSO crystal's PET scanner was modelled with 36.2 cm (7 rings) and 72.6 cm (14 rings) axial FOV. The outcomes indicated that the sensitivity and NECR values for the long-axial modelled PET scanner were 73% (77.6 kcps/MBq) and 42% (519 kcps) higher than the short-axial modelled PET scanner. In 2021, Samanta et al. utilized the GATE platform to develop a novel breast PET scanner. The detector geometry of this device was formed by two semicircles positioned on opposite sides, creating a rectangular shape, along with anterior and posterior panels. The result comparison indicated the sensitivity of the developer breast PET scanner was 3.21 times greater than that of the total body PET scanner under the same testing conditions (Samanta et al., 2021).

1.3. Research Gaps

Despite extensive research validating GATE for estimating the performance parameters of SPECT and PET systems, the specific codes from these studies remain unpublished. On the other hand, the simulation codes for the Mediso Any Scan S SPECT system and the General Electric (GE) Discovery-IQ PET system are not yet developed. Therefore, developing simulation codes is crucial for both monitoring the degradation of performance in these imaging systems over time and conducting other possible research. Additionally, to date, no comprehensive study has investigated the validation of GATE to assess the intrinsic performance parameters of the SPECT device at a 5 ≥ UFOV distance based on NEMA QC. In this regard, collimator optimization at various distances based on extrinsic NEMA QC is also unimplemented.

1.4. The Aim of Study and Novelty

This thesis aims to create simulation programs based on Monte Carlo methods for SPECT and PET systems using the GATE. In this context, simulation codes are being developed for the first time for both the dual-head Mediso Any Scan S SPECT system at SBÜ Trabzon Kanuni Education and Research Hospital and the GE Discovery-IQ PET imaging system at KTU Farabi Hospital International. Within this framework, validation of GATE was performed to estimate the performance parameters of both SPECT and PET scanners. In this regard, the experimental and simulation performance parameters were evaluated based on the NEMA QC test. For the SPECT, the extrinsic performance parameters were assessed at different distances. Additionally, the intrinsic performance parameters, spatial resolution, including energy resolution, and uniformity, were examined at a 5 ≥ UFOV distance.

The progress of biomedical imaging technology has led to an increase in the diversity and usefulness of collimators used in SPECT systems. In this context, manufacturers are persistently researching suitable geometric characteristics at tiny scales to minimise image noise caused by unwanted events. Accordingly, the geometric dimensional of the low-energy high resolution (LEHR), low-energy general purpose (LEGP), and high-energy general purpose (HEGP) collimators for the SPECT device were optimized depending on the collimator geometry dimensions for a couple of manufacturers (GE (General Electric Discovery), SI (Intevo Siemens), PS (Skylight Philips), GE400XCT (General Electric 400XCT), MG (General Electric Millennium), PB (Philips Brightview Camera), and GV (MillenniumVG Kameran).), which are illustrated in Table 1.

Table 1. Geometric features of collimators from the various manufacturers

Collimators	Hole length (mm)	Hole diameter (mm)	Septa thickness (mm)
GE-LEHR	35.0	1.50	0.20
SI-LEHR	24.05	1.11	0.16
PS-LEHR	32.8	1.40	0.15
SP-LEGP	24.7	1.40	0.18
GE400XCT-LEGP	41	2.5	0.30
MG-LEGP	43	2.5	0.25
MG-HEGP	48	3.4	1.65
PB-HEGP	58	3.81	1.73
GV-HEGP	66	4	1.8

Moreover, the intrinsic performance parameters for the SPECT scanner, which was modelled using different scintillation crystals listed in Table 2 at three different manufactured thicknesses (9.5 mm for low energy, 12.7 mm, and 15.8 mm for high energy), were assessed. To explore the potential of utilizing diverse scintillation crystal types at optimal thicknesses in a SPECT scanner.

Table 2. Inorganic scintillation crystal characteristics

Properties	Density ($g.cm^{-3}$)	LightYield (ph/keV)	Decay Time (ns)
GAGG	6.63	40-60	50-150
NaI(TI)	3.67	49	230
$LaCI_3$	3.79	49	28
CsI(TI)	4.51	54	900
$LaBr_3$	5.29	63	25
$YAIO_3$	5.4	25	28

On the other hand, based on the NEMA standards, the Tri-Sleeve PET Sensitivity Phantom (rTSSP-PET) and handcrafted NEMA scattering phantom were experimentally produced to measure the PET scanner performance parameters.

1.5. SPECT Device

SPECT is widely used among nuclear medicine imaging modalities in that it may offer information at both the functional and molecular levels (Wernick & Aarsvold, 2004). The essential idea of SPECT is that a radioactive isotope (radiopharmaceutical) is administered to the patient intravenously or via another acceptable route, and the isotope is absorbed by the targeted tissue or organ in the body (Peter, 2003). The device's detectors detect the isotope's gamma rays, which are then converted into three-dimensional images on a computer. This provides information not just on anatomical features, but also about the metabolic and physiological activities of tissues. The SPECT scanner operates within an energy range of 70 keV to 400 keV. Several detection event types are detected in the SPECT scanner, a number of which are invalid detections that contribute to image quality degradation. Invalid detections arise from the scattering of gamma rays within the patient's body and the scintillator, in addition to gamma rays that have penetrated the collimator septa (Prior & Lecoq, 2012). The desired valid detections are non-scattered events that pass through the collimator holes directly to the instrument's crystal (Herscovitch, 2014). The three main components that compose the SPECT scanner detector are a crystal, usually scintillation, a collimator, and finally a photomultiplier tube (PMT), as demonstrated in Figure 1.

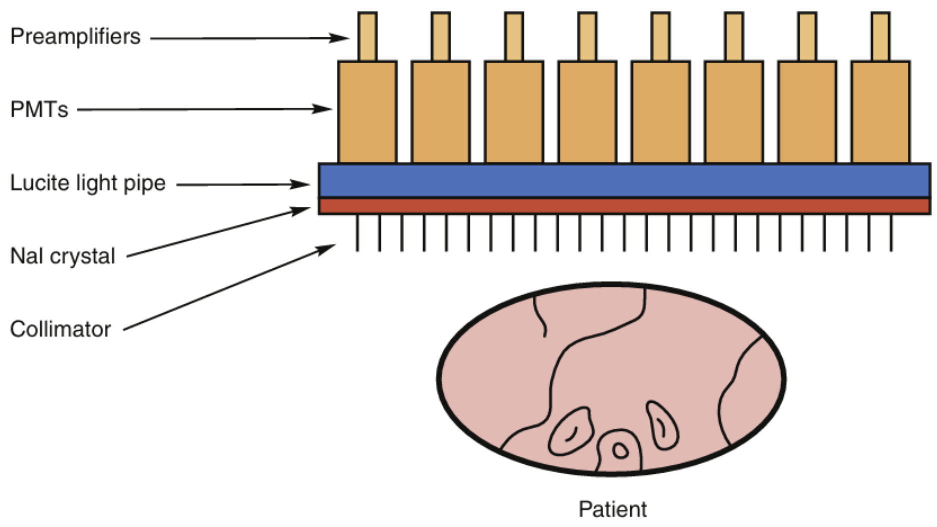

Figure 1. Schema of the SPECT instrument

1.5.1. Collimator

Collimators are an important part of nuclear medicine imaging technology. They are employed in SPECT devices and have a direct impact on the quality, resolution, and sensitivity of the images they produce (Moore et al., 1992). Collimators in SPECT systems manage the direction and number of photons that reach the gamma camera detectors (Weinmann et al., 2009). This process prevents undesirable scattering and interference signals from occurring. To achieve this objective, the collimators are constructed from materials that possess both high density and higher atomic numbers, such as lead, tungsten, and platinum (Gunter, 2004).

The design and type of collimators are influenced by various factors, including the imaging objective, target organ, radiopharmaceutical utilized, and detector technology (Noori-Asl & Jeddi-Dashghapou, 2022). In clinical applications, frequently used collimator types include parallel-hole collimators, convergent collimators (fan-beam and cone-beam), divergent collimators, and pinhole collimators; these collimator types are represented in Figure 2.

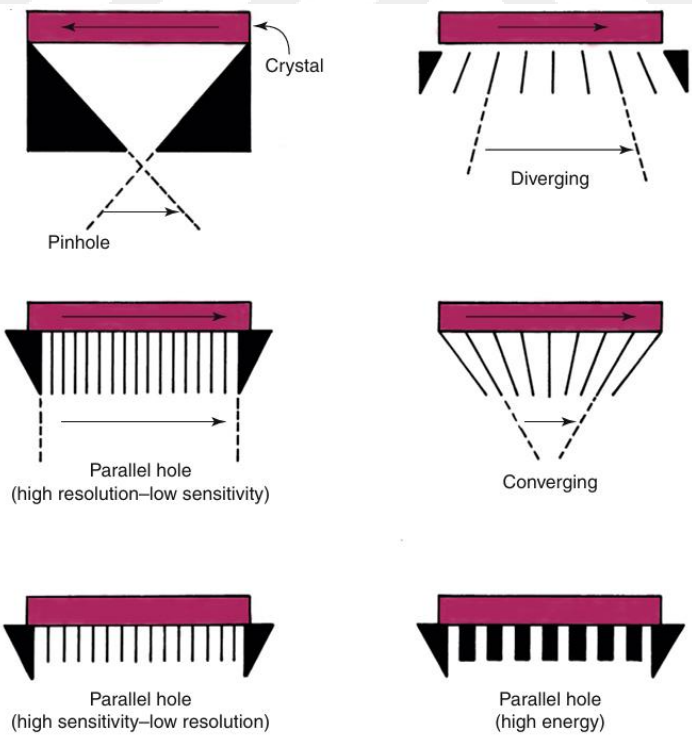

Figure 2. Common collimator types

Parallel-hole collimators are among the most frequently utilised types of collimators in SPECT devices, preferred for a diverse range of clinical and research applications

(Weinmann et al., 2009). Based on the gamma energy of the radioisotopes used in the pharmaceutical, both the hole geometric dimension (hole length and diameter) and the septa thickness of the parallel collimator are varied. Depending on these, the parallel hole collimators are categorised as low energy high resolution (LEHR), low energy general purpose (LEGP), medium energy general purpose (MEGP), high energy general purpose (HEGP), and low energy high sensitivity (LEHS). The gamma energy ranges for the parallel hole collimator are categorised as low (70 keV - 160 keV), medium (160 keV - 250 keV), and high (250 keV - 400 keV) (Van et al., 2015).

The septa thickness, hole diameter, and hole length, as well as the source-to-collimator distance, directly affect the geometric spatial resolution $R_{coll}$of the parallel hole collimators (Gregory et al., 2017); therefore, these two parameters for the parallel hole collimator with diameter D and hole lengths L at T distance from the point source, are given by the Eq. (1).

$$R_{coll} = \frac{D(T + L)}{T} \tag{1}$$

1.5.2. Scintillators and Photomultiplier Tubes

The objective of the SPECT scanner's scintillator crystal is to transform the single gamma ray that reaches it from the patient's body into visible light. The energy of photons interacting with a crystal via one of the interaction types—such as Compton interactions or photoelectric effects is absorbed in this process (Kim et al., 2021). This process causes the atom's electrons to change into a higher energy level, which results in the atom's excitation (Xu et al., 2024). Electrons release the excess energy as visible light via electrons to return to a lower level. Often, inorganic scintillation crystals are used for the SPECT scanner, such as Na(TI), BGO, LSO, GSO, LYSO, and Cs(TI) (Peterson & Furenlid, 2011). These crystals should possess specific physical properties, like high stopping power, high energy resolution, and high efficiency, as well as additional requirements, which are low hygros-copicity, chemical and mechanical stability, thermal stability, and ease of crystal fabrication. To reduce absorption and make the lateral light distribution as predictable as feasible, the SPECT scanner's crystal structure is built from a large single crystal. The thickness of the crystal is another geometric factor that affects the sensitivity and spatial resolution; it is 9.5 mm for low energy and 12.7 mm or 15.8 mm for high energy (Xu et al., 2024).

The visible photons that are generated from the crystal are incident on the array of PMTs, which convert them into a set of pulses. PMTs consist of a photocathode, dynodes, and an anode within a vacuum tube of glass (Hautefeuille et al., 2021). The photoelectrons are emitted from the photocathode as a result of visible light striking. Photoelectrons are emitted from the photocathode due to the impact of visible light. As a result, the analog pulses become digital after going through the preamplifier, linear amplifier, pulse-height analyzer, and analog-to-digital conversion (ACD) (Prior & Lecoq, 2012).

1.6. PET Device

1.6.1. Physics in PET Device

PET is a significant nuclear tomography technique that relies on the radioactive decay properties of radioisotopes for its functional mechanism. The PET technique relies on the positron-emitting decay process to create 3D images of cellular activity or certain organ functions within the patient's body (Robilotta, 2004). This imaging is performed by detecting the back-to-back gamma radiation that is emitted as a result of positron annihilation after the decay process of a radionuclide (Kijewski, 2016). Generally, the radioisotopes with a low neutron/proton (*N/Z*) ratio, known as proton-rich isotopes, convert one of their protons into a neutron to achieve a stable level. As a result of this decay process, a positron and a neutrino are ejected from nuclei. The total quantity of energy released in decay is distributed among the daughter nucleus, the emitted positron, and the associated neutrino (Bailey et al., 2005). Thus, the positron particle loses all its energy within a short distance of propagation through medium matter and combines with an electron to produce two photons with 511 keV energy (Shukla & Kumar, 2006). The positron emission process and annihilation event are illustrated in Figure 3.

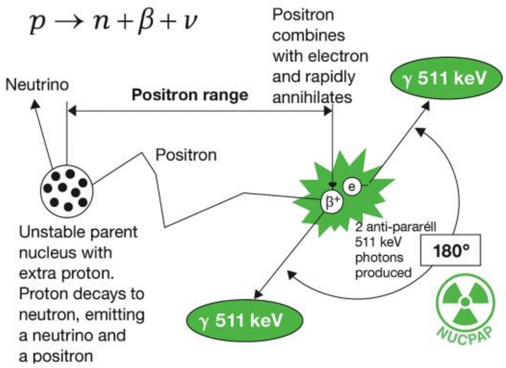

Figure 3. Positron emission process and annihilation event (Cherry et al,. 2003)

1.6.2. PET Detector

The PET scanner detection system is composed of an enormous number of scintillation crystal pixels. As demonstrated in Figure 4, the crystal pixels are engineered as an array in cubic or rectangular blocks (Bailey et al., 2005). The block-pixelated crystals are constructed in multiple rings to detect back-to-back photons produced by annihilation events at the same time. The scintillators are linked with photosensor arrays to collect the visible light that is produced by gamma-ray interaction with scintillators. The scintillation crystals utilized in PET scanners must have specific physical characteristics to ensure optimal performance. The properties involve high atomic density, effective atomic number, significant light output, and rapid decay time. These provide a high efficiency, excellent energy and spatial resolution for PET scanners (Saha, 2011).

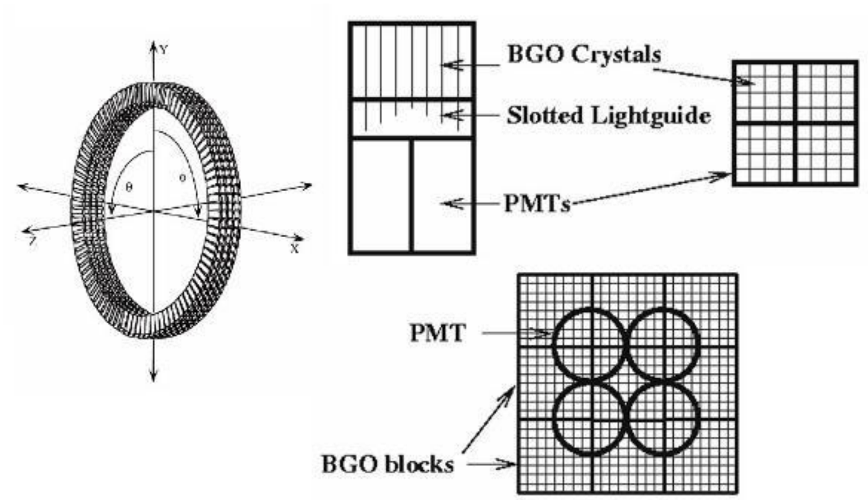

Figure 4. Schematic of PET scanner (D. L. Bailey et al., 2005)

The detection of photons that are emitted simultaneously is known as a coincidence event. The short time interval that this event is registered within, called the coincidence window, is about a few nanoseconds. Generally, a PET scanner registers three types of events, which are true, random, and scattering, as shown in Figure 5 (Kijewski, 2016). True events result from photons with 511 keV within a coincidence window, generated from the same annihilation event. Random events occur when photons are created by different annihilation events. In contrast, scattering events are caused by photons that were recorded from the identical annihilation events but suffered Compton interaction inside the region of interest (Basu et al., 2011).

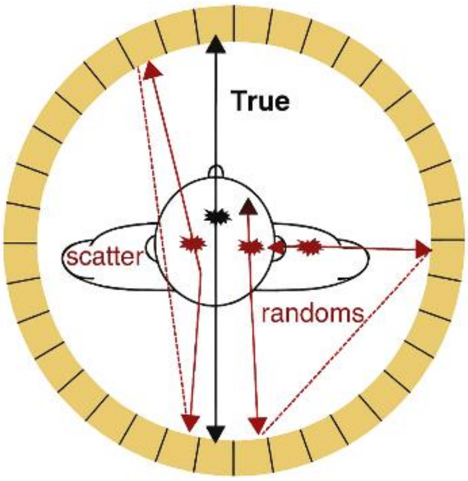

Figure 5. Coincidence evevnts in PET scanner (Kijewski, 2016)

1.7. Monte Carlo Simulation

Monte Carlo simulations (MC) are stochastic methods that employ random numbers and statistical sampling techniques to approximate solutions to different mathematical problems (Loudos, 2007). The random sampling approach was employed in nuclear physics from a quantum mechanics viewpoint, which interprets matter-radiation interactions as probabilities (Buvat & Castiglioni, 2002). Monte Carlo simulates the physical interactions between particles and matter by modelling the trajectory of particles, photons, and charged particles via a sequence of geometric shapes (Sarrut et al., 2021). Due to the stochastic nature of radiation emissions, transports, and detection processes, analytical modelling is essential for assessing various parameters in medical imaging systems. The Monte Carlo method is applicable for addressing problems related to statistical processes. Its utility is especially pronounced in the field of medical imaging physics, given the stochastic characteristics associated with radiation emission, transport, and detection processes.

There are two types of Monte Carlo codes, generic and specific are used in simulations for nuclear medicine applications. Generic codes are designed to handle radiation in matter. Nonetheless, these codes are rarely employed in the field of nuclear medicine. Modelling of complex gamma camera components presents challenges related to geometry definition, and the default cross-sections used in the code could not offer sufficient accuracy for applications in nuclear medicine.

Emission tomography uses packages for tracking many photons and particles. Monte Carlo (MC) methods, such as EGS, MCNP, FLUKA, Penelope, and GEANT4, are among them. These programs may be limited since they take a long time to run when working with complicated imaging equipment, but they can make realistic models of how particles interact with matter (I. Buvat & Castiglioni, 2002; Irene Buvat & Lazaro, 2006; Loudos, 2007). For these cases, specialized simulation software specifically designed for photon tracking in emission tomography is generally preferred. Several simulation platforms based on the GEANT4 platform have been developed for both PET and SPECT, such as GATE, SimSET, SIMIND, SimSPECT, PETSIM, Eidolon, GRAY/GAMOS, and GATE (Karine Assié et al., 2004). The main drawbacks of some Monte Carlo package codes are the potential lack of support over time, limitations in physics description, and issues with maintenance, support, and upgrades.

1.8. General Performance Parameters of Imaging Devices

1.8.1. Sensitivity

The sensitivity is defined as the number of valid events detected per selected time frame and radioactive source activity (Desmonts et al., 2020). These events are represented by unscattered photons within a specified energy window for the SPECT scanner, whereas they are true events within the coincidence window in the PET scanner (İnce et al,. 2021). The Eq. (2) expresses this parameter.

$$Sensitivty = \frac{Number\ of\ detected\ photons\ (cps)}{Radiosource\ activity} \tag{2}$$

1.8.2. Spatial Resolution

The capacity of the gamma cameras to determine the smallest distance between two spots on the surface of the image is termed system spatial resolution (Weng et al,. 2016). In general, the spatial resolution of gamma cameras is evaluated as the full width at half maximum (FWHM) by a Gaussian fitting of the point or line spread function, as indicated in Eq. (3).

$$FWHM = 2\sqrt{2ln2}\sigma \approx 2.35\sigma \tag{3}$$

In the SPECT scanner, the system's spatial resolution ($FWHM_{sys}$) encompasses the spatial resolutions of the imaging device's components, which are the collimator resolution ($FWHM_{coll}$) along with intrinsic resolution ($FWHM_{int}$), which includes both crystal and electronics, as indicated in Eq. (4) (Bhatia et al., 2015).

$$FWHM_{SYS} = \sqrt{FWHM_{coll}^2 + FWHM_{int}^2} \tag{4}$$

Usually, the FWHM for the SPECT scanner is measured using a special quadrant bar phantom. For the more accurate evaluation of the device's ability to resolve phantom patterns, the FWHM and the modulation transfer function (MTF) are assessed based on the pre-empirical approach of Hander et al. (1997). This approach depends on the Fourier transform of a normalized line spread function LSF(nLSF), Eq. (6).

$$MTF(f) = \left| \int_{-\infty}^{+\infty} nLSF(x)e^{-2\pi ifx}dx \right| \tag{5}$$

where n is a normalization constant. The MTF is computed from the LSF employing Eq. (5), assuming that the Gaussian function represents the LSF.

$$MTF(f) = e^{-2\pi^2\sigma^2f^2} \tag{6}$$

The parameters σ and f in Eq. (6) refer to the standard deviation and spatial frequency, respectively, with their values connected to the FWHM and the phantom's bar frequency f_b as outlined.

$$\sigma = \frac{FWHM}{2.35} \tag{7}$$

$$f_b = \frac{1}{2 \times bar\ width} \tag{8}$$

The MTF (f_b) in Eq. (9) can be obtained by applying Eqs. (7) and (8) into Eq. (6).

$$MTF(f_b) \approx e^{-0.894\left(\frac{FWHM}{bar\ width}\right)^2} \tag{9}$$

By using the MTF predicted value from Hander et al. (1997) and solving Eq. (9), the FWHM is determined by the following equation.

$$FWHM \approx 1.058 \times bar\ width \cdot \sqrt{\ln\left[\frac{\mu(f_b)}{\sqrt{2} \cdot \sigma(f_b)}\right]} \tag{10}$$

The mean value as well as the standard deviation of the counts per pixel in a region of interest (ROI) are represented by the variables $\mu(f_b)$ and $\sigma(f_b)$. Sixteen shades of gray are discernible to the human eye, indicating that the threshold of contrast resolution is somewhere between 1/15 and 1/16. Substituting this value in Eq. (10), the FWHM becomes equal to Eq. (11) (Ashoor & Khorshidi, 2023; Hander et al., 1997; Wasserman, 1998).

$$FWHM = 1.75 \times bar\ width \tag{11}$$

1.8.3. Energy resolution

Energy resolution refers to the scintillation crystal's ability to discriminate between gamma-ray photons of various energies. The mathematical term for energy resolution (R) is $(\triangle E)$, referring to the FWHM of the gamma-ray photopeak divided by the centroid photopeak energy $(E_\circ)$, corresponding to the energy of the detected gamma-ray. In general, the intrinsic energy resolution of the PET and SPECT devices could be represented as Equation (12), which is the combination of several parameters that affect the gamma-ray energy peak output in the absence of a collimator in the case of a SPECT instrument.

$$R = R_{sc} + R_p + R_{st} \tag{12}$$

where the intrinsic resolution of the crystal is represented by R_{sc}, the transfer resolution by R_p, and the PMT resolution by R_{st}. For identical scintillation crystals, the scintillator summation of $R_{sc} + R_p = 0$. Therefore, the following equation represents the energy resolution:

$$R = (\frac{\Delta E}{E_\circ})^2 = R_{st} \tag{13}$$

Using the Gaussian statistical model to estimate the fractional variance of signals, the PMT (R_{st}) yields a resolution of:

$$R_{st} = 2.335 \times \sqrt{\frac{1-\varepsilon}{N}} \tag{14}$$

where N refers to the quantity of photoelectrons and ε signifies the variance of the electron multiplier gain, respectively. In this context, the intrinsic resolution of scintillation detectors (R) is defined as follows:

$$R = 2.335 \times \frac{\sigma}{E_\circ} = \frac{FWHM}{E_\circ} \tag{15}$$

The symbols σ and $E_\circ$ represent the standard deviation and mean energy of the complete energy peak, respectively, while FWHM represents the full-width half maximum of the energy peak (Dorenbos et al., 1995; Moszyński, 2003; Moszyński et al., 2016; Moszyński et al., 2002; Salgado et al., 2022; Zanzonico, 2013).

1.8.4. Uniformity

The parameter known as uniformity determines the camera's response to uniform irradiation on the detector surface. The intrinsic uniformity assessment is based on a pair of variables. The first, called intrinsic integral uniformity (IU), describes how the detector responds to uniform radiation throughout both the useful field of view (UFOV) and the center field of view (CFOV). The second, termed differential uniformity (DU), quantifies the detector's response to homogeneous radiation over small, adjacent areas for the CFOV and UFOV. The calculation of the two mentioned uniformity variables is performed using Eqs. (16) and (17), respectively.

$$IU = \frac{Co_{max} - Co_{min}}{Co_{max} + C_{omin}} \times 100\% \tag{16}$$

$$DU = \frac{H_{count} - L_{count}}{H_{count} + L_{count}} \times 100\% \tag{17}$$

where, Co_{max} and Co_{min} represent the maximum and minimum pixel counts, respectively, within the designated field of view (FOV). The H_{count} and L_{count} denote the highest and lowest counts, respectively, calculated from five adjoining pixels (Elkamhawy et al., 2000; Hasan et al., 2017; H. C. Kim, Kim, Kim, Lee, & Lee, 2017).

1.8.5. Count performance

Count performance reflects the ability of a tomography to accurately detect valid events in changing radioactivities. In the case of a PET scanner, it reflects the capacity to differentiate among true, random, and scattered events. Nevertheless, the count rate cannot provide direct information about the magnitude of the signal-to-noise ratio. The noise equivalent count rate provides this information via the following formula.

$$NECR = \frac{C_T^2}{C_T + C_S + C_R} \tag{18}$$

The true, scatter, and random coincidence counting rates are denoted as C_T, C_S, C_R, respectively (Hallen et al., 2020; Lu et al., 2016).

2. MATERIAL AND METHODS

The validation of the GATE platform to assess experimentally measured performance parameters for the SPECT and PET scanners was conducted in this thesis. For this purpose, the experimental measurements of extrinsic and intrinsic performance for the dual-head Mediso Any Scan S SPECT scanner were performed in the first step. For the GATE modelling of the SPECT scanner, which relies on its physical characteristics, the validation of the GATE platform for extrinsic and intrinsic performance parameters was implemented in the second step. Experimental measurements and simulation predictions of performance factors for the SPECT scanner were conducted based on the NEMA-NU 2007 quality control tests. Additionally, the collimator optimization (three parallel hole collimators) for the SPECT scanner simulated with the NaI(TI) crystal, and intrinsic performance parameters for SPECT scanners simulated with different scintillation crystals were investigated. In the third step, experimental phantom preparation was done, and performance parameters of the GE Discovery-IQ PET scanner were measured. Furthermore, the GATE modeling of the GE Discovery-IQ PET scanner and validation of its performance prediction were investigated.

2.1. Experimental Measurements of SPECT Scanner Performance

2.1.1. Extrinsic Performance Parameters

(1) System Planar Sensitivity. The experimental, planar system sensitivity test for the SPECT imaging system using LEHR, LEGP, and HEGP collimators was performed at five different distances from the planar phantom, which are 10 cm, 15 cm, 20 cm, 25 cm, and 30 cm. Two types of radioisotopes were used in this test. The first is the ^{99m}Tc for the LEHR and LEGP collimators, while the second is the ^{131}I isotope for the HEGP collimator. The phantom in this test is a plastic cylindrical phantom (Petri dish) with an internal diameter of 9.8 cm, an external diameter of 10 cm, and a depth of 1.2 cm filled with 1 mCi of isotope. As illustrated in Figure 6, the cylinder phantom is put under the wood MDF disc with a thickness of 8 mm and a diameter of 30 cm, perforated from its centre as a disc with a diameter of 9 cm. The acquisition parameters like time, energy window, matrix size, and zoom factor for the SPECT scanner were set at 100 s, 512×512, 20%, and 1.03515 pixel/mm, respectively. The NMQC plugin of the ImageJ software was used for data analysis.

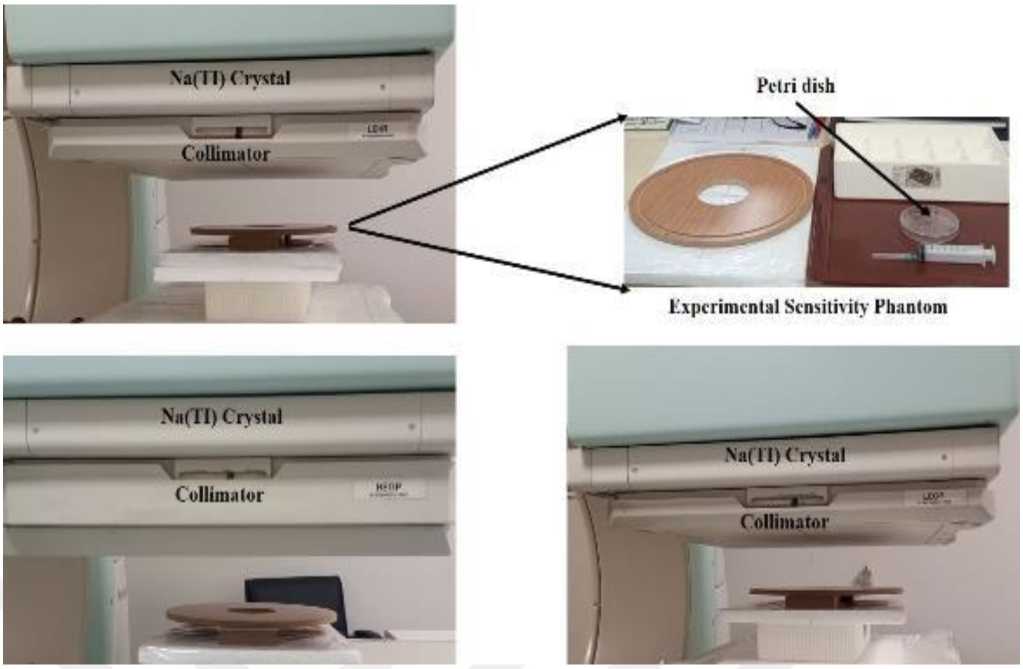

Figure 6. Experimental testing of planar sensitivity for the SPECT scanner

(2) System Spatial Resolution. The system's spatial resolution was assessed for the SPECT scanner using LEHR, LEGP, and HEGP collimators. The phantom preparation involves using four microhematocrit capillary tubes with a length of 7.5 cm and an internal diameter equal to 1.1 mm. These capillary tubes are filled with 2 mCi of ^{99m}Tc isotope for LEHR and LEGP collimators, as well as about 1.5 mCi of ^{131}I isotope for the HEGP collimator. As illustrated in Figure 7, capillary tubes (line source) are arranged on the paper in a square shape, and each tube is separated from the other by 10 cm. Consequently, the paper is installed on a piece of Styrofoam with a thickness of 2 cm and dimensions of 30 cm × 30 cm. The manufacturer's acquisition factors for this test were a count of 100000, a 20% energy window, and a matrix size of 512×512 with a zoom factor of 1.03515 pixels/mm. The FWHM of the LSF, obtained by image profile peaks, is analyzed using the NMQC plugin of ImageJ software.

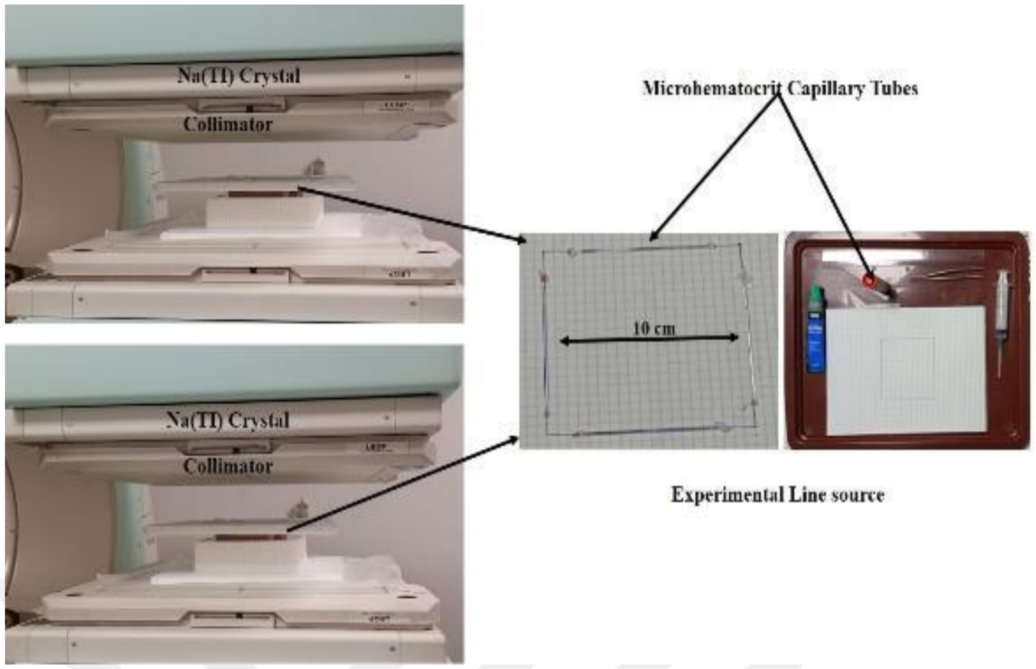

Figure 7. Practical test of system spatial resolution for the SPECT scanner

2.1.2. Intrinsic Performance Parameter

(a) Intrinsic Spatial Resolution. This parameter is experimentally measured using a quadrant bar phantom composed of four patterns. Each pattern consists of a group of lead bars with the same width. These lead bars are separated by distances that are equal to the lead bar width at a specific pattern. As shown in Figure 8, the lead bar widths are 2 mm, 2.5 mm, 3 mm, and 3.5 mm. The quadrant bar phantom is installed above the SPECT scanner detector without a collimator. As indicated in Figure 8, at a distance of ≥ 5 UFOV from the center of the SPECT detector surface, a point source ^{99m}Tc (140 keV) radioisotope with 0.5 mCi/cc (1 mCi in 2 cc) activity and a count rate of 24000 cps is fixed. The intrinsic spatial resolution test was performed at 8 million counts using the SPECT scanner's default manufacturer’s acquisition parameters, which are a 20% energy window and a 512 × 512 × 16 matrix size. To obtain vertical and horizontal images for different bar widths relative to each part of the SPECT device’s crystal, the data acquisition was repeated eight times. The MTF (modulation transfer function) for each phantom's pattern and the FWHM for the smallest eye resolvable lead bar width were estimated using ImageJ software.

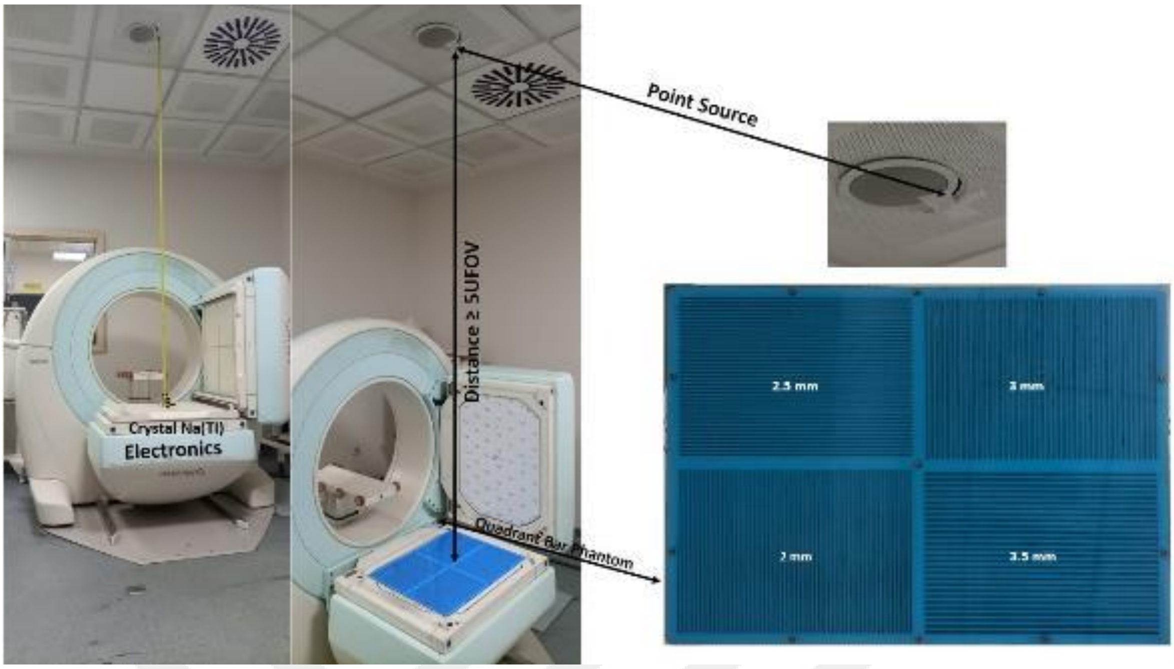

Figure 8. Experimental testing of intrinsic spatial resolution

(b) Intrinsic Energy Resolution. The high-energy and low-energy intrinsic resolution tests for the dual-SPECT heads (Detector 1 and Detector 2) were done. An injector filled with 0.31 mCi/cc (0.62 mCi in 2 cc) of ^{99m}Tc radioactive material, which has a count rate of 31000 cps, was used as a point source for the low-energy resolution test. In contrast, the injector filled with 0.25 mCi/cc (0.50 mCi in 2 cc) of ^{131}I radioactive material with a count rate of 18000 cps was used as a point source for the high-energy resolution test. As demonstrated in Figure 9, each point source is installed at a distance of $\geq$ 5 UFOV from the center without collimation of the SPECT detector surface at each test. The default manufacturer's acquisition parameters for the SPECT scanner that was used in these tests are 20%, 256 × 256 × 16, and 66000 counts for the energy window, matrix size, and count number, respectively. The peaks' data extracted using the pydicom library from obtained DICOM outputs were analyzed to calculate the energy resolution capability for the SPECT scanner relative to low and high energies.

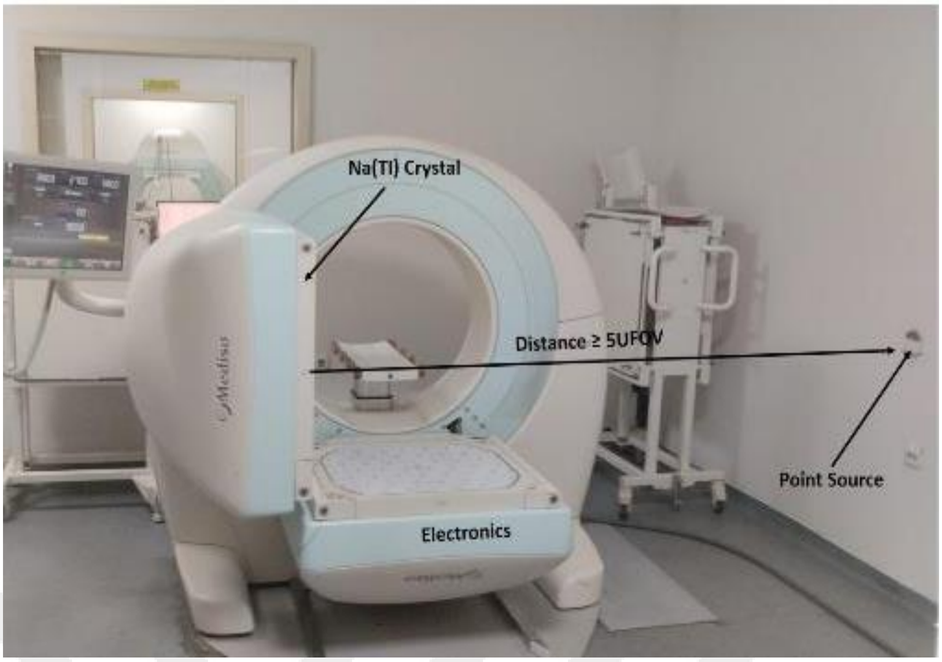

Figure 9. Practical testing of energy resolution and uniformity for the SPECT scanner

(c) Intrinsic Uniformity. As illustrated in Figure 9, the differential and integral intrinsic uniformity for the useful field of view (UFOV) and for the center field of view (CFOV) of the dual SPECT head scanner were measured. The uniformity experiment test was performed by applying a similar energy resolution procedure and the same acquisition parameters. However, this test was performed at the 16 million count using an injector that contained 0.25 mCi/cc (0.5 mCi in 2 cc) of ^{99m}Tc as a point source with a 24000 cps count rate.

2.2. GATE

GATE is a GEANT4 library-based, editable Monte Carlo simulation platform developed for modeling equipment used in nuclear medicine. The features of GEANT4 libraries, including time-dependent processes and source distributions, provide the GATE platform with enhanced capabilities for more realistic simulation of imaging device components like SPECT and PET (Sarrut, 2022). Three distinct layers compose the structure of the GATE platform, each of them offers unique benefits for the user. The initial layer is the core layer, which offers essential tools for geometry definition, time management, source specification, data digitization, and output generation. The second layer is the application layer, which enhances the core layer by including specialized features and expanding its capabilities. The last layer is the user layer. It provides a convenient interface for configuring and performing simulations. Constructing the simulation model for the scanner requires implementing several steps (Verdonck, 2008). A couple of them are main steps, which are explained as follows (GATE Collaboration, 2025):

The first step is creating the physical environment space for the simulation model, which is called the “world volume”. This volume is a physical space that involves the volumes of all objects included in the simulation. The geometrical definition step includes constructing the geometric shapes and defining the geometric dimensions for objects (detectors, sources, and phantoms) that are required to simulate imaging devices. Additionally, the material type of the objects and their location inside the environment are identified (OpenGATE Collaboration, 2025).

The other step is the physics list, which provides all interaction likelihoods for both photons and charged particles with matter. The physics list constructors of GEANT4 are utilized by the GATE simulation platform. The constructors include the standard model, low energy, the Livermore model, and the Penelope model. Each model includes a specific charged particle list (γ-rays, x-rays, optical photons, muons, hadrons, positrons, and electrons) and their interactions (Rayleigh scattering, photoelectric effect, Compton scattering, ionization e^- and e^+, bremsstrahlung e^- and e^+, and e^+ annihilation). The standard and the Livermore packages employ the mathematical fitting of experimental data and low-energy experimental data, respectively. The Penelope package relies on the Penelope code data. The common electromagnetic standard constructors are EmStandard opt0, EmStandard opt2, EmStandard opt3, and EmStandard opt4 (Apostolakis, 2007; Arce et al., 2021; Ivanchenko et al., 2011).

Afterward, the energy deposition caused by the interaction of virtual particles with a sensitive detector material is conserved as hits. These hits are filtered through a sequence of series modules to convert them into digital singles. The adder module collects the generated hits within a specified crystal volume. The energy deposition caused by the interaction of virtual particles with a sensitive detector material is conserved as hits. These hits are filtered through a sequence of series modules to convert them into digital singles. The adder module collects the generated hits within a specified crystal volume. This unit is followed by a readout module to regroup the pulses from the different volumes. The readout module is a virtual volume linked to the sensitive volumes (crystals), offering two different methods that approximately correspond to the APD and PMT blocks, which are the winner-takes-all and energy-centroid approaches, respectively. Additional modules that may enhance the digitizer series include energy and spatial blurring, as well as the Thresholder/Upholder modules that assist in identifying the energy windows. Additional units, such as coincidence and delayed windows, are inserted into the digitizer chain of the PET scanner to organize the singles list for coincidence events (Jan et al., 2011; Jan et al., 2004). The produced singles can be stored in a ROOT output file that contains the output singles for each applied unit, as shown in Figure 10.

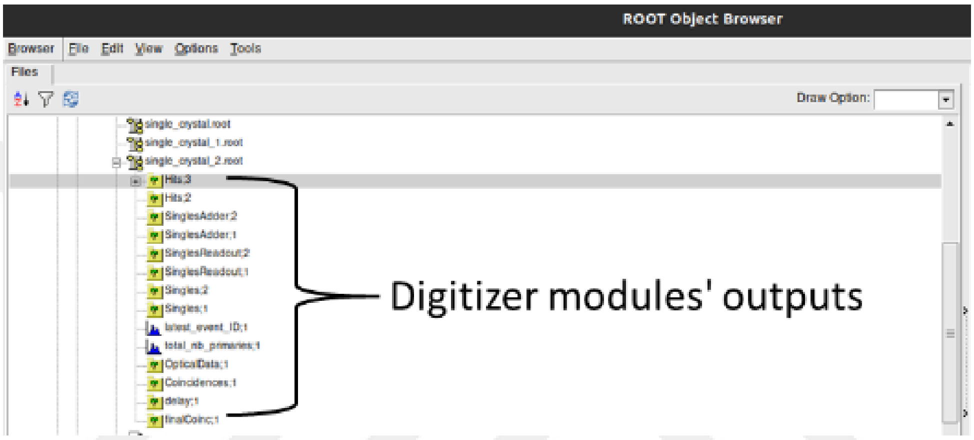

Figure 10. Root output of GATE

2.3. GATE Modelling of SPECT Scanner and Validation

This section of this thesis presents the validation of the GATE platform to simulate the geometric model of the SPECT scanner and predict the experimentally measured extrinsic performance parameters for the SPECT scanner. In this regard, the GATE steps mentioned above for modelling the imaging device were applied to modelling dual-head Mediso Any Scan S SPECT scanner. Within this framework, the physical environment, the components of the SPECT head, the physics interaction package, the digitizer chain, the output data, and the image projection were modeled by following the steps.

2.3.1. Modelling of the SPECT Scanner

The physical environment that is referred to as the world in the GATE platform was defined with X, Y, and Z dimensions equal to 5 m, along with its material for the simulation model, as demonstrated in Figure 11.

Within the second step, the components of the SPECT scanner, which include three different types of parallel hole collimators (LEHR, LEGP, and HEGP), NaI(TI) scintillation crystal, and a back compartment, were mimicked, as illustrated in Figure 12. The SPECT scanner was simulated according to the physical specifications of the dual-head Mediso Any Scan S SPECT device presented in Table 3.

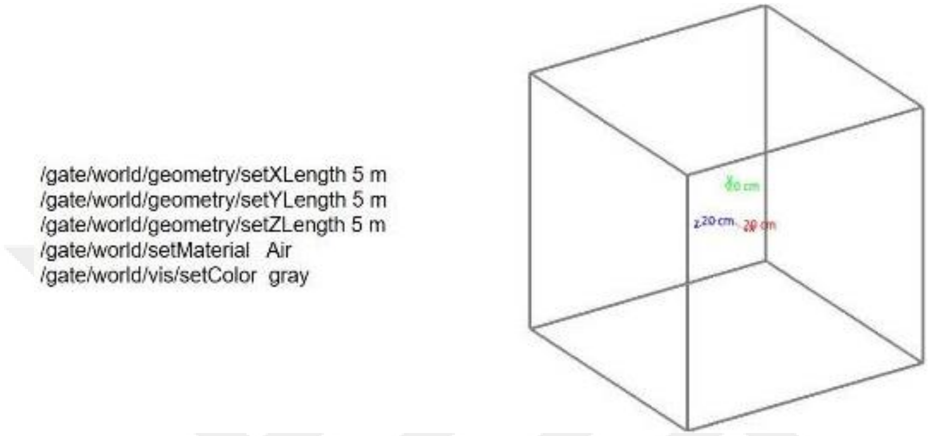

Figure 11. Simulation of physical space (World)

Table 3. Mediso Any Scan S SPECT device physical specifications

Detector			
FOV (mm)	585×470		
Crystal			
Thickness (mm)	9.5		
Scintillator	NaI(TI)		
Collimators	LEHR	LEGP	HEGP
Holeshape	Hexagonal	Hexagonal	Hexagonal
Hole length (mm)	35	35	55
Hole diameter (mm)	1.5	1.9	3.4
Septa thickness (mm)	0.16	0.2	1.6
Material	Lead	Lead	lead

```
# SPECT HEAD
/gate/world/daughters/name SPECThead
/gate/world/daughters/insert box
/gate/SPECThead/geometry/setXLength 69.5 mm
/gate/SPECThead/geometry/setYLength 562 mm
/gate/SPECThead/geometry/setZLength 680 mm
/gate/SPECThead/placement/setTranslation 0. 0. 0. mm
/gate/SPECThead/setMaterial Air
# COLLIMATOR
/gate/SPECThead/daughters/name collimator
/gate/SPECThead/daughters/insert box
/gate/collimator/geometry/setXLength 35 mm
/gate/collimator/geometry/setYLength 562 mm
/gate/collimator/geometry/setZLength 685 mm
/gate/collimator/placement/setTranslation 17.25 0. 0.  mm
/gate/collimator/setMaterial Lead
/gate/collimator/daughters/name hole
/gate/collimator/daughters/insert hexagone
/gate/hole/geometry/setHeight 35 mm
/gate/hole/geometry/setRadius 0.75 mm
/gate/hole/setMaterial Air
/gate/hole/repeaters/insert cubicArray
/gate/hole/cubicArray/setRepeatNumberX 1
/gate/hole/cubicArray/setRepeatNumberY 265
/gate/hole/cubicArray/setRepeatNumberZ 191
/gate/hole/cubicArray/setRepeatVector 0. 1.66 2.875  mm
/gate/hole/repeaters/insert linear
/gate/hole/linear/setRepeatNumber 2
/gate/hole/linear/setRepeatVector 0.  0.83 1.44  mm
# CRYSTAL
/gate/SPECThead/daughters/name crystal
/gate/SPECThead/daughters/insert box
/gate/crystal/geometry/setXLength  9.5 mm
/gate/crystal/geometry/setYLength  470 mm
/gate/crystal/geometry/setZLength  585 mm
/gate/crystal/placement/setTranslation  5. 0.  0. mm
/gate/crystal/setMaterial Na(TI)
# ELECTRONICS
/gate/SPECThead/daughters/name electronics
/gate/SPECThead/daughters/insert box
/gate/electronics/geometry/setXLength  25 mm
/gate/electronics/geometry/setYLength  470 mm
/gate/electronics/geometry/setZLength  585 mm
/gate/electronics/placement/setTranslation 22.25 0.0. mm
/gate/electronics/setMaterial glass
```

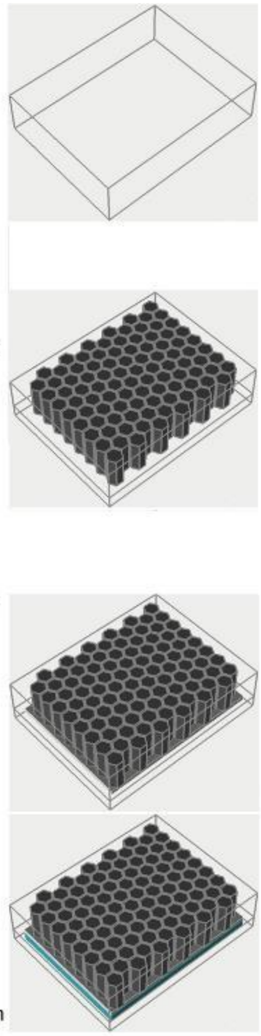

Figure 12. Simulation model of Mediso Any Scan S SPECT scanner

The EmStandard Opt4 constructor was utilized to manage the physical process for the SPECT scanner simulation model. This constructor involves various combinations of physics packages, and a couple of these that are implemented in the simulation SPECT scanner are Livermore, Standard, LowEP Compton, and Penelope. The initialization step consists of just one command line that implements the initiation of the previous steps. The required radioactive source for the specific test is modeled directly after the initialization step. In this step, the two-point and four-line radioactivity sources for the ^{99m}Tc radioisotope, along with the one-point and four-line radioactivity sources for the ^{131}I radioisotope that were utilized in the SPECT scanner's quality control tests, were simulated (Appendix 1).

The output data for each digitizer model with ROOT format and the image projection data, along with pixel size, matrix size, time frame, and acquisition start, were set up, respectively. Figure 13 demonstrates the command-line code for the physics list, the radioactive source, and the initialization command lines, respectively.

```
#PHYSICSLIST
/gate/physics/addPhysicsList      emstandard_opt4
#INITIALIZATION
/gate/run/initialize
#SOURCE
/gate/source/addSource   Name
/gate/source/Name/gps/particle   gamma
/gate/source/Name/gps/ang/type iso
/gate/source/Name/gps/type Volume or Point
/gate/source/Name/gps/type Mono
/gate/source/Name/gps/ene/mono ##   keV
/gate/source/Name/setActivity        ## becquerel
#OUTPUT
/gate/output/root/enable
/gate/output/root/setFileName  output
/gate/output/root/setRootHitFlag  1 or 0
/gate/output/root/setRootSinglesAdderFlag  1 or 0
/gate/output/root/setRootSinglesSpblurringFlag 1 or 0
/gate/output/root/setRootSinglesBlurringFlag 1 or 0
/gate/output/root/setRootSinglesSpblurringFlag 1 or 0
/gate/output/root/setRootSinglesThresholderFlag 1 or 0

#IMAGE PROJECTION
/gate/output/projection/enable
/gate/output/projection/setFileName
/gate/output/projection/pixelSizeX  ## mm
/gate/output/projection/pixelSizeY  ## mm
/gate/output/projection/pixelNumberX ##
/gate/output/projection/pixelNumberY ##

#TIME FRAME
/gate/application/setTimeSlice     # s
/gate/application/setTimeStart     # s
/gate/application/setTimeStop     # s
#RUN THE SIMULATION
/gate/application/start
```

Figure 13. GATE command lines for the physics list, initialization process, radioactive source configuration, and output settings

The diagram in Figure 14 illustrates the different stages of the artificial digitizer model for the SPECT scanner, which were constructed utilizing features of the digitizer modules available on the GATE platform. The electronics digitizer modules include the adder, readout, crystal blurring (which consists of Crystal Resolution Min and Crystal Resolution Max), spatial blurring, and threshold electronics. The energy blurring setting range is 7% to 10% for 364.5 keV and 9% to 11% for 140.5 keV for tests assessed with high and low energies. The macro codes of the digitizer steps module for the SPECT device model are illustrated in Appendix 2.

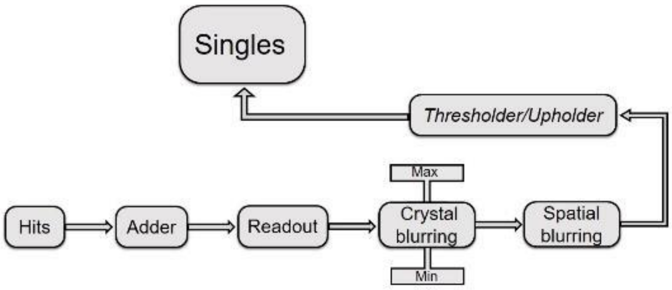

Figure 14. Digitizer modules of a simulated SPECT scanner

2.3.2. Validation of GATE for Extrinsic Measurements

The validation capability of GATE for evaluating the extrinsic performance of the modelled dual-head Mediso Any Scan S SPECT scanner using the same acquisition parameters (acquisition time, energy window, matrix size, count rates, and count number) in experimental measurements was implemented. In this context, the Petri dish phantom required for the planar sensitivity test and the four-line phantom arranged in a square shape for the system spatial resolution test were simulated. These phantoms are modeled utilizing a ^{99m}Tc radioactivity source for parameters tested with LEHR and LEGP collimators, in contrast to a ^{131}I radioactivity source for parameters examined with the HEGP collimator. The test models for the system's spatial resolution and planar sensitivity were mimicked at various distances (10 cm, 15 cm, 20 cm, 25 cm, and 30 cm), as shown in Figure 15.

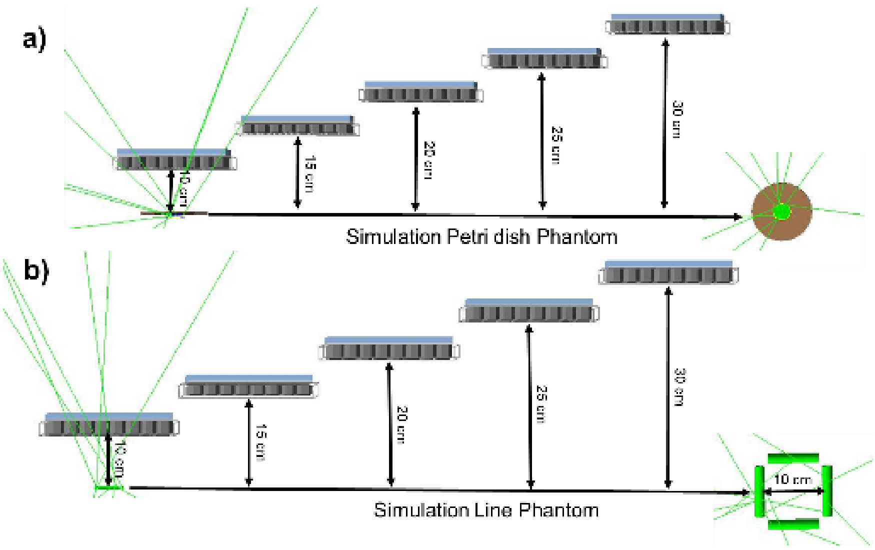

Figure 15. Simulation model of a) a planar sensitivity test and b) a system spatial resolution test

2.3.3. Collimator Optimization

The optimal geometrical dimensions for the LEHR, LEGP, and HEGP collimators were investigated by evaluating the extrinsic performance parameters of various SPECT scanner simulation models at a 10 cm distance. For this purpose, fifteen different simulation models of each collimator were implemented. More specifically, collimators with three different diameters (1.48 mm, 1.5 mm, and 1.52 mm for LEHR; 1.88 mm, 1.9 mm, and 1.92 mm for LEPG; and 3.38 mm, 3.4 mm, and 3.42 mm for HEGP) were utilized to estimate the performance parameters (sensitivity and spatial resolution (FWHM)) of the modeled SPECT system. Each diameter was used at five different hole lengths. The whole length varies from 35 mm to 37 mm for collimators LEHR and LEGP, while for collimator HEGP, it ranges from 55 mm to 57 mm, with a 0.5 mm difference between each. Moreover, the acquisition factors of the testing model (acquisition time, energy window, matrix size, count rates, and count number) were identified as experimental and validation tests. The obtained outputs from optimization and validation tests were analyzed by ROOT software.

2.3.4. GATE Validation of Intrinsic Measurements

The GATE validation of the intrinsic performance assessment for the without-collimator modelled dual-head Mediso Any Scan S SPECT scanner was performed. For this objective, the testing models for the intrinsic spatial resolution, intrinsic energy resolution, and intrinsic uniformity, along with the necessary phantoms for each model, were simulated in a manner similar to the models used for experimental measurement.

(a) Intrinsic Spatial Resolution. As shown in Figure 16, the simulation model of the quadrant bar phantom that was used for the experimental evaluation of intrinsic spatial resolution was implemented. This phantom is made of an epoxy material box composed of four patterns. Each pattern contains a certain number of lead strips with the same dimensions and thickness, which are indicated in Figure 16 and Appendix 3. The simulated phantom was positioned above the SPECT scanner model detector at a distance ≥ 5 UFOV from a ^{99m}Tc simulated point radioactive source with 1 mCi activity. The same experimental methodology was used for the output data analysis to predict the MTF and FWHM values for the SPECT scanner simulation model.

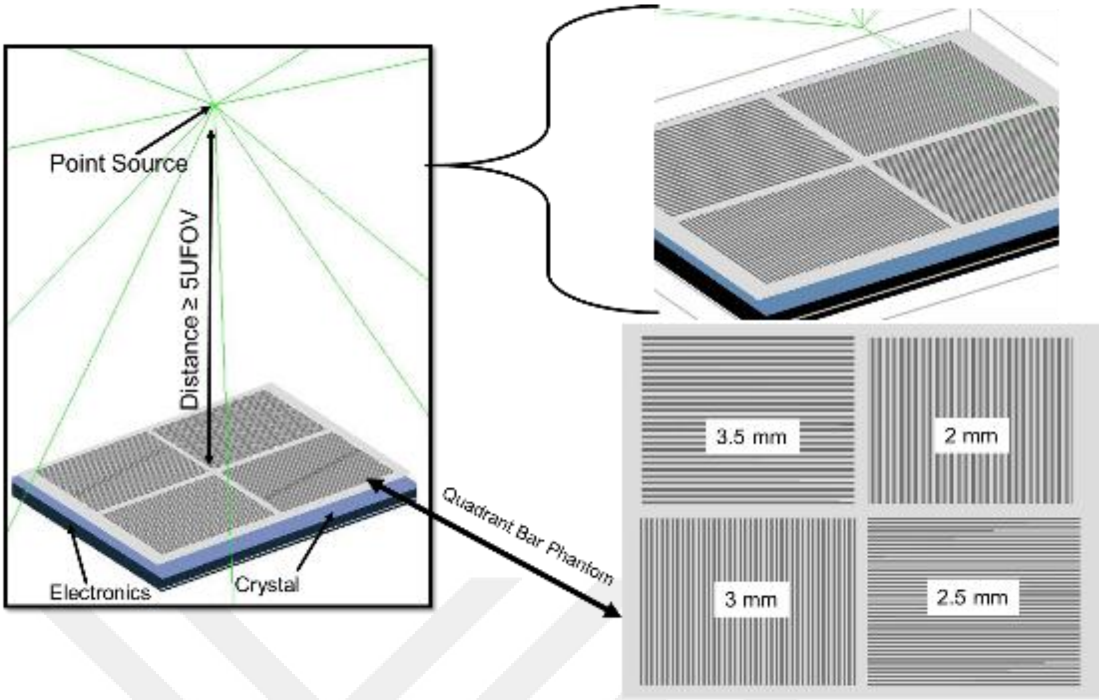

Figure 16. Simulation model of intrinsic spatial resolution using ^{99m}Tc radioisotope

(b) Intrinsic Energy Resolution and Intrinsic Uniformity. The SPECT scanner's simulation models for intrinsic energy resolution at 140 keV and 364.5 keV, as well as for the intrinsic uniformity, were executed. In this framework, the ^{99m}Tc point source for the low-energy resolution test and a ^{131}I point source for the high-energy resolution were modeled. The simulated ^{99m}Tc point source was utilized in both the low-energy resolution and intrinsic uniformity parameters tests, while a ^{131}I point source was used for the high-energy resolution parameter assessment. The point sources' positions and their decay activities, in addition to acquisition parameters for each test, were identified according to a practical testing model. The ROOT output data documents were analyzed with the ROOT software to calculate the low- and high-energy resolution parameters, whereas the output obtained from the uniformity test was analyzed with the NMQC plugin of ImageJ software to evaluate the DU and IU. Figure 17 illustrates the simulation models of the energy resolution test.

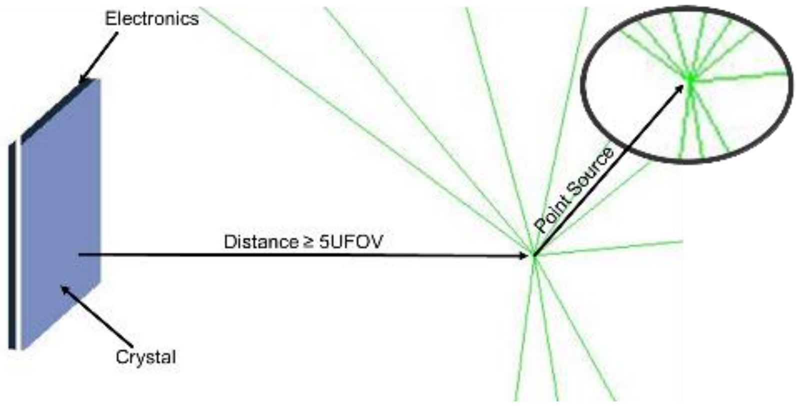

Figure 17. Simulation model of intrinsic energy resolution and uniformity

2.3.5. GATE Evaluation of Intrinsic Performance for Various SPECT Scanners

In this framework, the evaluation of intrinsic performance parameters for the SPECT scanner model was simulated with NaI(TI), GAGG, CsI(TI), $LaBr_3$, $LaCI_3$, and $YAOI_3$ scintillation crystals using three standard crystal thicknesses, which are 9.5 mm, 12.7 mm, and 15.8 mm. Manufacturers already use the chosen thicknesses at low and high energies on SPECT scanners. Accordingly, in addition to the SPECT scanner model with a 9.5 mm NaI(Tl) scintillation crystal thickness, seventeen SPECT scanner models were simulated. Utilizing a high-energy radioactive source, the intrinsic spatial resolution and intrinsic energy resolution parameters were evaluated for the SPECT scanners modeled with 12.7 mm and 15.8 mm thickness crystals. The intrinsic uniformity parameter, along with two other parameters, was assessed for the SPECT scanners designed with 9.5 mm-thick crystals using a low-energy radioactive source.

(1) Intrinsic Spatial Resolution. A previously simulated quadrant bar phantom was utilized to test the intrinsic spatial resolution for the SPECT models with 9.5 mm-thick crystals (NaI(TI), GAGG, CsI(TI), $LaBr_3$, $LaCI_3$, and $YAIO_3$). The radioactivity amount of the ^{99m}Tc point source, as well as all acquisition parameters at the experimental measurement, were applied in these tests. On the other hand, ^{131}I point radioactive sources were used to assess this factor for the SPECT scanner modeled with 12.7 mm and 15.8 mm crystals (NaI(TI), GAGG, CsI(TI), $LaBr_3$, $LaCI_3$, and $YAIO_3$) thicknesses. Due to a high penetration of gamma photons with energies greater than 140 keV to the 3.25 mm thick lead bars, a special configuration to assess the intrinsic spatial resolution for the SPECT scanners

modeled with 12.7 mm and 15.8 mm thickness of crystals, utilizing ^{131}I point sources (364.5 keV), was simulated.

The configured model, illustrated in Figure 18 and Appendix 4, comprises a lead block containing five slits of various widths arranged consecutively. The dimensions of the lead block are 40 × 43 × 5.5 cm, which corresponds to both the SPECT scanner model's FOV and the thickness of the HEGP collimators. The implementation of this thickness reduces the direct penetration of gamma photons to the lead block. While slit widths are 1.5 mm, 2 mm, 2.5 mm, 3 mm, and 3.5 mm, each measures 18 cm in length, with an 8 cm separation between slits to prevent gamma ray penetration. This lead block was located anterior to the SPECT scanner detector.

To conserve gamma emission in narrow beams and ensure that each slit on a lead block has uniform gamma radiation access, a special source holder was simulated. The modeled source's holder is a lead box that measures 47 × 12 × 5.5 cm; five cylindrical holes are positioned within it in horizontal form. Each cylindrical hole has a height of 5 cm and a diameter of 1 mm, coupled to a point ^{131}I source with an activity of 0.20 mCi. The acquisition is carried out at 60000 counts, and the source holder was situated at a distance of $\geq$ 5 UFOV. Using ImageJ software, the FWHM was estimated for each slit by analyzing the peaks of the image profile.

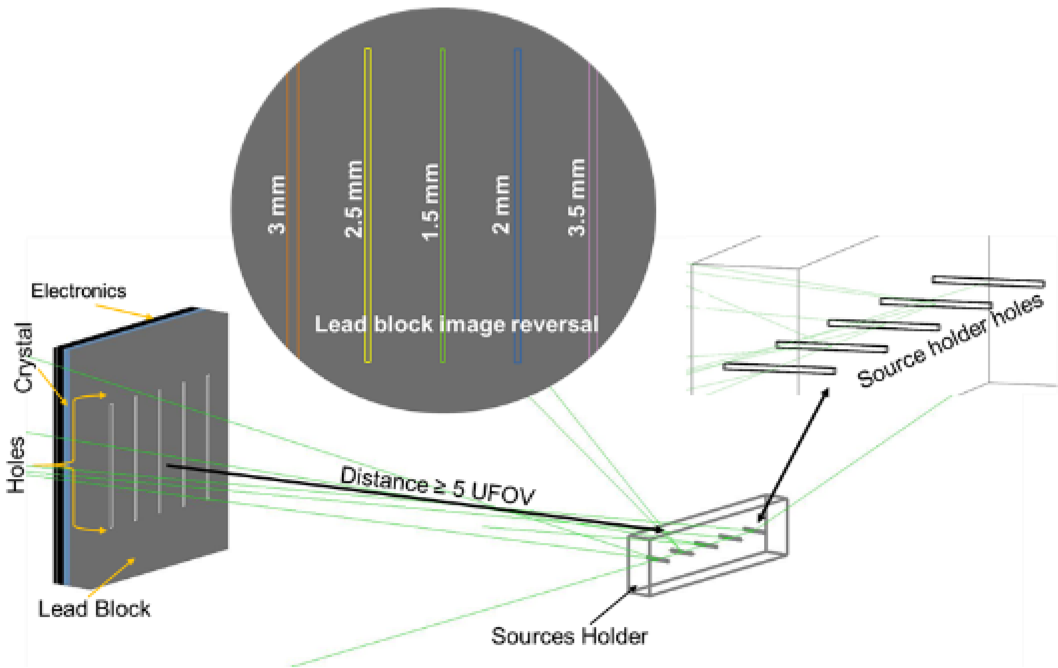

Figure 18. Simulation model of intrinsic spatial resolution using ^{131}I radioisotope

(2) Intrinsic Energy Resolution and Intrinsic Uniformity. The intrinsic energy resolution and intrinsic uniformity were assessed for the SPECT scanner by employing different scintillation crystals. Utilizing the same testing model for validating the intrinsic energy resolution parameter demonstrated in Figure 17, this parameter for SPECT scanner models simulated with various scintillation crystals and thicknesses was estimated. More specifically, for the crystals mentioned above, a low-energy ^{99m}Tc point radioactive source was used for the 9.5 mm thick crystals; in contrast, a high-energy ^{131}I point radioactive source was used for the crystals at 9.5 mm, 12.7 mm, and 15.8 mm thicknesses. On the other hand, the DU and IU intrinsic uniformity parameters of the CFOV and UFOV were estimated just for the SPECT models with 9.5 mm thick scintillation crystals. The intrinsic parameter tests were conducted by applying the same acquisition parameters, in addition to data output analysis software, as the validation tests.

2.4. Experimental Measurement of PET Scanner Performance

This section presents the experimental measurements of quality control test parameters for the GE PET Discovery QI scanner and the phantoms' assembly required for these measurements. In this context, the sensitivity and count performance parameters were measured according to NEMA quality control tests. Using the data analysis software of the GE PET Discovery IQ, the outputs from experimental measurements were analyzed.

2.4.1. Sensitivity

The sensitivity was evaluated according to the NEMA NU2-2012 quality test. In this test, the Redesigned Tri-Sleeve PET Sensitivity Phantom (rTSSP-PET) was used instead of the five sleeves that comprised aluminium tubes, each 700 mm long with a wall thickness of 1.25 mm and varying diameters. The rTSSP-PET was constructed using three aluminium sleeve tubes, each measuring 700 mm in length. The tubes have wall thicknesses of 1.25 mm and 2.5 mm, as shown in Figure 19. The sensitivity parameter was measured by arranging these three aluminium tubes five times. For each thickness, the linear phantom was positioned at the center of the transaxial field of view and again at a distance of 10 cm from the transaxial field of view to conduct the sensitivity quality control experiment. The linear phantom contained 130 μCi of ^{18}F, and the sensitivity was calculated.

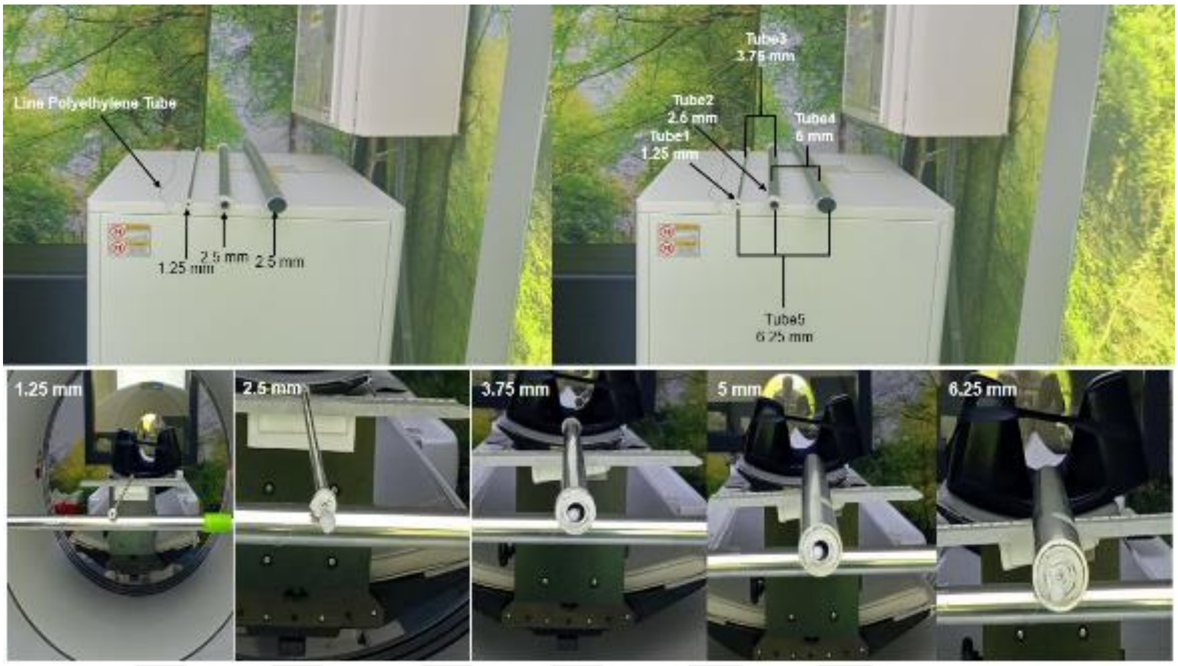

Figure 19. Experimental testing of sensitivity for the PET scanner

2.4.2. Count Performance

As shown in Figure 20, a handcrafted NEMA scattering phantom was used in the performance test for count rate. This phantom is made of three cylindrical pieces of high-density (0.96 ± 0.01 g/cm) polyethylene, each one with a 20 cm diameter and a 25 cm length. As demonstrated in Figure 21, a plastic line source with a 3.2 mm internal diameter, 4.8 mm outside diameter, and 730 mm length is positioned 45 mm offset from the transaxial axis of the NEMA scatter phantom. The plastic line source is filled with 8.36 mCi of ^{18}F isotope, which corresponds to 13.3 kBq/mL, and the test was performed in two phases. The first phase consists of ten frames, with each lasting 15 minutes, while the second phase includes 25 frames that last 25 minutes.

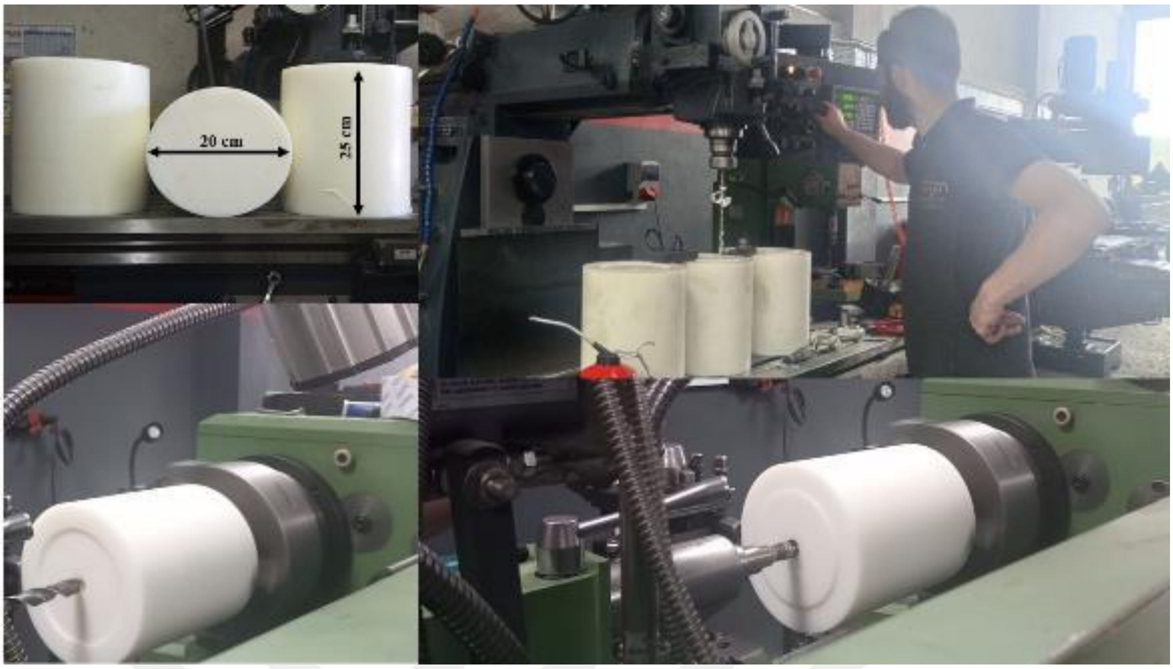

Figure 20. Production of a NEMA scattering phantom

Figure 21. Practical testing of a count performance for the PET scanner

2.5. GATE Modelling of PET Scanner and Validation

Applying the GATE MC platform steps to modeling imaging devices, the simulation model of the GE Discovery-IQ PET scanner was implemented according to the device's physical properties. In this regard, the PET scanner's detector, digitizer modules, radioactive sources, and phantoms that were utilized in the validation test were modeled. Furthermore, the GATE platform validation for the estimation of sensitivity and count performance parameters was performed. By modifying the special C^{++} code presented in the GATE code, the ROOT outputs data for the two evaluation tests were analyzed.

2.5.1. Modelling of the PET Scanner

The geometry definition step includes simulation models for the physical environment and the PET detector. The simulation model's physical environment was constructed as explained in the SPECT scanner simulation model. Using the physical characteristics of the GE Discovery-IQ PET scanner in Table 4, the PET detector was simulated, and the modeling steps are indicated in Figure 22. Additionally, this step involves modeling the required phantoms for validating performance parameters, as will be detailed in the validation section.

Table 4. Physical characteristics of the GE Discovery-IQ PET scanner

Detector	
Transaxial field of view (mm)	700
Ring diameter (mm)	740
Axial field of view (mm)	155
Crystal	
Scintillator	BGO Bismuth Germanium
Scintillator dimension (mm)	6.3 × 6.3 × 30
Number of detector rings	3
Number of scintillators per block	8 × 8
Number of detector units per ring	36
Coincidence window	9.5 ns
Energy threshold	425 keV

```
#ECAT
/gate/world/daughters/name ecat
/gate/world/daughters/insert cylinder
/gate/ecat/setMaterial Air
/gate/ecat/geometry/setRmax 38 cm
/gate/ecat/geometry/setRmin 35 cm
/gate/ecat/geometry/setHeight 26 cm
/gate/ecat/vis/forceWireframe
/gate/ecat/vis/setColor white
#BLOCK
/gate/ecat/daughters/name block
/gate/ecat/daughters/insert box
/gate/block/placement/setTranslation  36.5. 0. 0 cm
/gate/block/geometry/setXLength 30. mm
/gate/block/geometry/setYLength 5.04 cm
/gate/block/geometry/setZLength 5.04 cm
/gate/block/setMaterial Air
/gate/block/vis/setColor white


#CRYSTA
/gate/block/daughters/name crystal
/gate/block/daughters/insert box
/gate/crystal/geometry/setXLength 30.0 mm
/gate/crystal/geometry/setYLength 6.3 mm
/gate/crystal/geometry/setZLength 6.3 mm
/gate/crystal/setMaterial BGO
/gate/crystal/vis/setColor yellow
#REPEAT  CRYSTAL
/gate/crystal/repeaters/insert cubicArray
/gate/crystal/cubicArray/setRepeatNumberX 1
/gate/crystal/cubicArray/setRepeatNumberY 8
/gate/crystal/cubicArray/setRepeatNumberZ 8
/gate/crystal/cubicArray/setRepeatVector 0.  6.5  6.5 mm


#REPEAT  CRYSTAL
/gate/crystal/repeaters/insert cubicArray
/gate/crystal/cubicArray/setRepeatNumberX 1
/gate/crystal/cubicArray/setRepeatNumberY 8
/gate/crystal/cubicArray/setRepeatNumberZ 8
/gate/crystal/cubicArray/setRepeatVector 0.  6.5  6.5 mm
#REPEAT  BLOCK
/gate/block/repeaters/insert linear
/gate/block/linear/setRepeatNumber 3
/gate/block/linear/setRepeatVector 0. 0. 5.04  cm
/gate/block/repeaters/insert ring
/gate/block/ring/setRepeatNumber 36
```

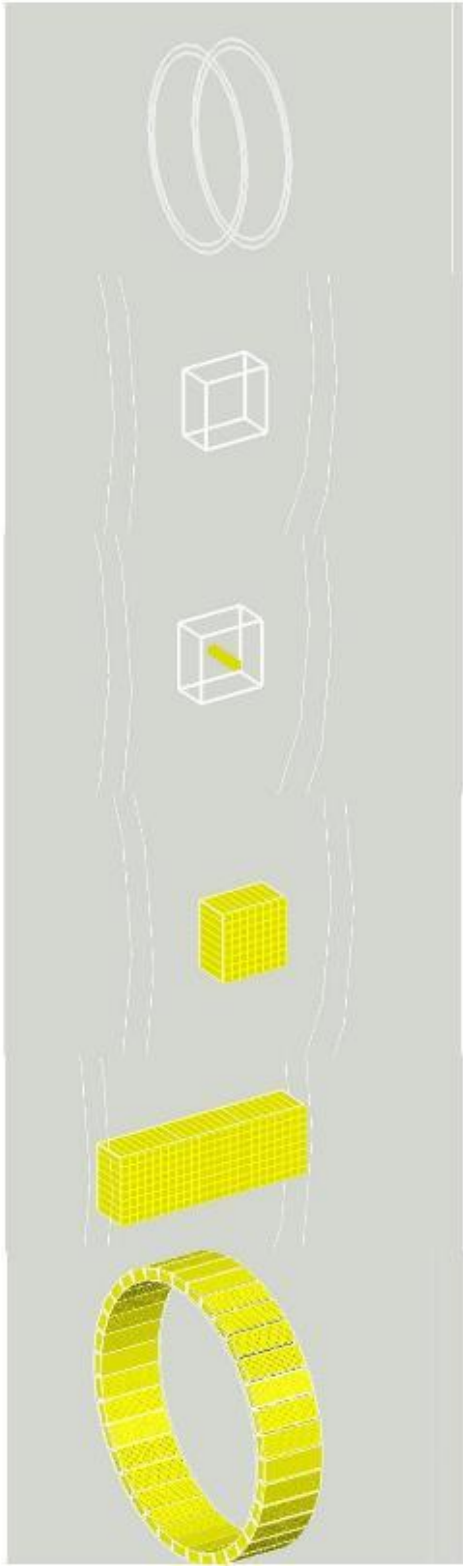

Figure 22. Simulation model of the GE Discovery-IQ PET scanner

Subsequently, as previously indicated in Figure 13, the physics list, the initialize command line for the geometric construction, the required radioactive source, the output data format, and the time frame settings were identified. Prior to defining the output data format and the time frame settings, the digitizer chain for the PET scanner is simulated. As indicated in Figure 23, the signal processing model of the PET device includes the dead time module, coincidence store module, and delay window module, in addition to the modules that consist of the SPECT device's digitizer modules.

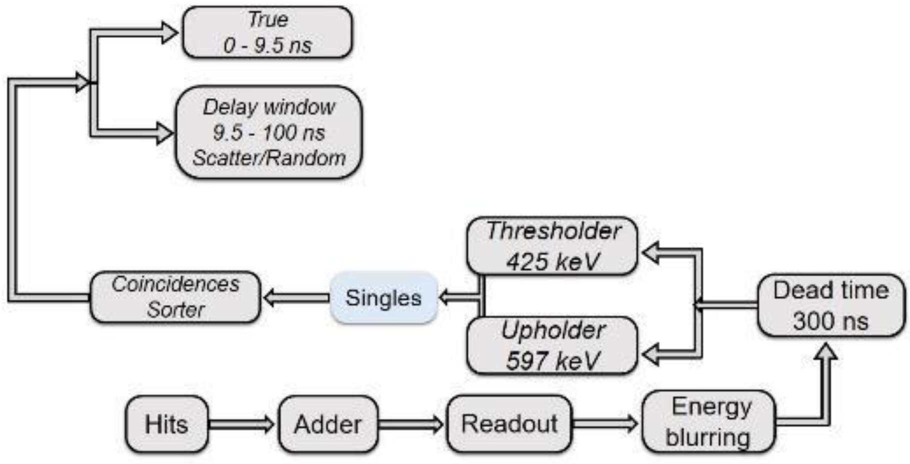

Figure 23. Digitizer modules of a simulated PET scanner

2.5.2. Validation Tests

(a) Sensitivity. The sensitivity parameter validation for the PET model was performed according to the NEMA NU2-2012. This verification was done by implementing the same experimental measurement procedure with the model of the standard NEMA sensitivity phantom. Five aluminum sleeve tubes, each with a 1.25 mm thickness and a 700 mm length with varying internal diameters (3.9 mm, 7.0 mm, 10.2 mm, 13.4 mm, and 16.4 mm), constitute the NEMA sensitivity phantom. The evaluation used a polyatlin tube model filled with 130 µCi of ^{18}F radioactivity, which has a 1.5-mm internal diameter, a 3.2-mm external diameter, and a length of 700 mm. As indicated in Figure 24, the ^{18}F radioactive source is inserted at the center of the first aluminum sleeve tube that has an internal diameter of 3.9 mm. Afterwards, the other sleeves gradually increase, starting from a small diameter to a larger one. The data acquisitions, with five separating frames of 1 minute each, were launched for each sleeve's thickness.

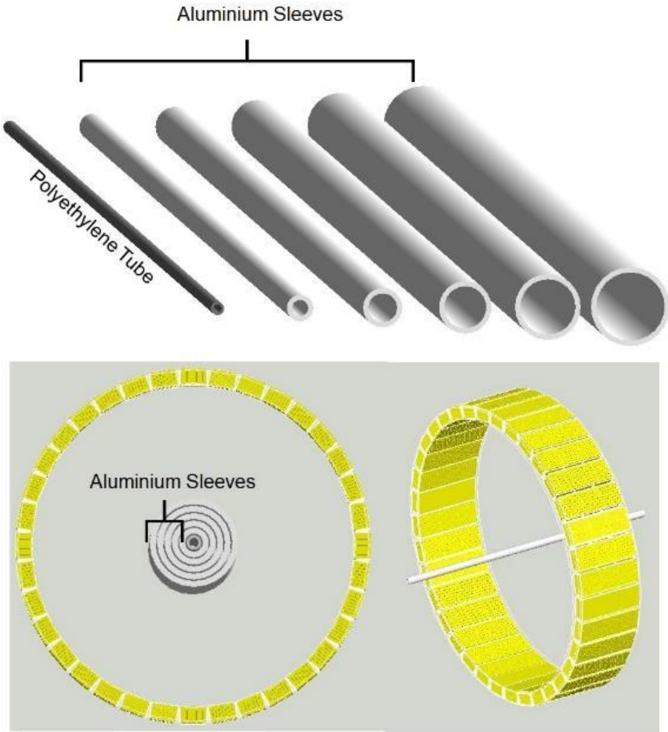

Figure 24. Simulation testing model of sensitivity for the PET scanner

(b) Count Performance. The evaluation count performance for the PET scanner model was assessed by simulating the practical test model. To reduce the simulated data acquisition time in this test, the cylindrical scattering phantom dimension and activity decay of the radioactivity source were minimized. In this regard, a plastic serum tube that is 15.5 cm long and contains an 1.76 mCi ^{18}F radioactivity source was placed inside a cylindrical scattering polyethylene phantom that is the same length and has a diameter of 20 cm, as illustrated in Figure 25. This procedure maintains the radioactivity concentration, equivalent to the experimental radioactivity concentration ranging from 13.3 kBq/mL to 2 kBq/mL. The acquisition of data was performed in two phases: the initial phase included 10 time frames, each one with 15 minutes, while the second time frame consisted of 25 frames, each one with 25 minutes.

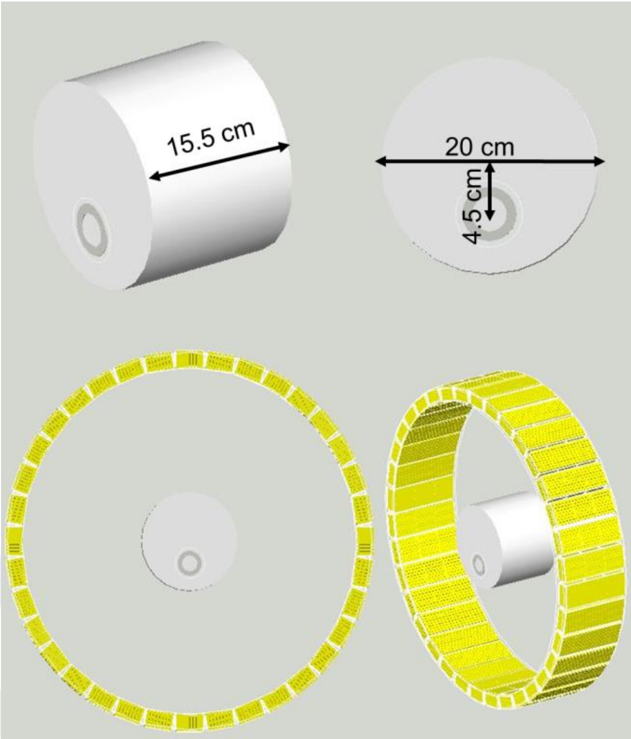

Figure 25. Simulation testing model of count rate for the PET scanner

3. RESULTS AND DISCUSSION

This thesis investigated the validity of the MC GATE platform for estimating the performance parameters of SPECT and PET scanners. To achieve this, first, the experimental measurements of the extrinsic sensitivity and spatial resolution were done using LEHR, LEGP, and HEGP collimators, as well as the intrinsic parameters, including spatial resolution, energy resolution, and intrinsic uniformity. Afterward, the parameters (extrinsic and intrinsic) are estimated for the simulation of the SPECT scanner model and compared with both the experimental and manufactured values. Furthermore, an investigation of the optimum dimension of collimators as well as the intrinsic parameters of various scintillator crystals for the SPECT model was conducted. Finally, the investigated sensitivity and performance count parameters for the PET scanner model were compared with both the experimental and the manufacturer's values.

3.1. Extrinsic Performance Parameters for SPECT

3.1.1. Validation

The experimental and simulation results of planar sensitivity as well as system spatial resolution using LEHR, LEGP, and HEGP collimators at different distances from the phantom are illustrated in Figure 26 and Figure 27. Overall, it was observed that the sensitivity values (from experiments and simulations) for the SPECT scanner were almost unaffected by increasing distance for all collimators used. This finding is due to the influence of the ratio of collimator holes to the source-to-collimator distance. On the other hand, the deterioration in the experimental and simulation values of FWHM under the same conditions is caused by the increase in the spread angle of gamma rays.

With a variance of 4.7%, 2.3%, and 8.4% for LEHR, LEGP, and HEGP collimators, respectively, the simulated predictions of system sensitivity at a distance of 10 cm nearly matched the experimental data. However, with the identical collimators, the deviation values increased to 9.7%, 6.8%, and 25%, respectively, at a distance of 30 cm.

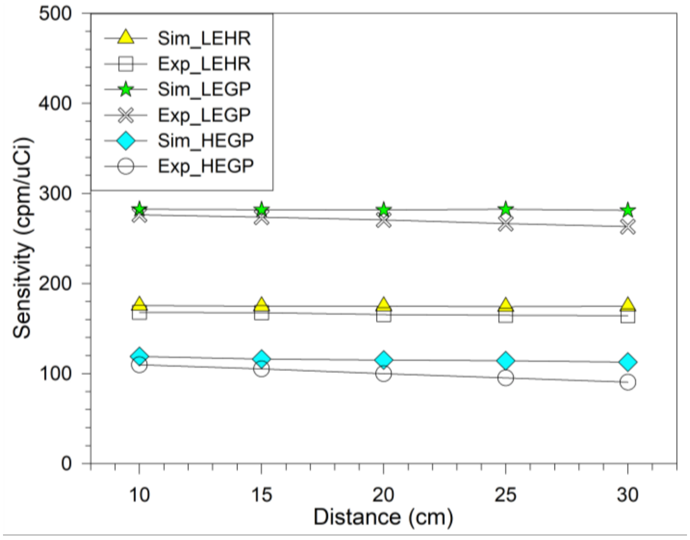

Figure 26. Experimental and simulation values of planar sensitivity for SPECT

Likewise, when the distance was increased from 10 cm to 30 cm, the FWHM for the LEHR collimator varied between 3% and 5.5%, for the LEGP collimator it varied between 1.7% and 4%, and for the HEGP collimator it ranged from 0.55% to 6.5%. The differences between experimental and simulated FWHM values for the LEHR, LEGP, and HEGP collimators at a 10 cm distance are 0.35 mm, 0.15 mm, and 0.071 mm, respectively.

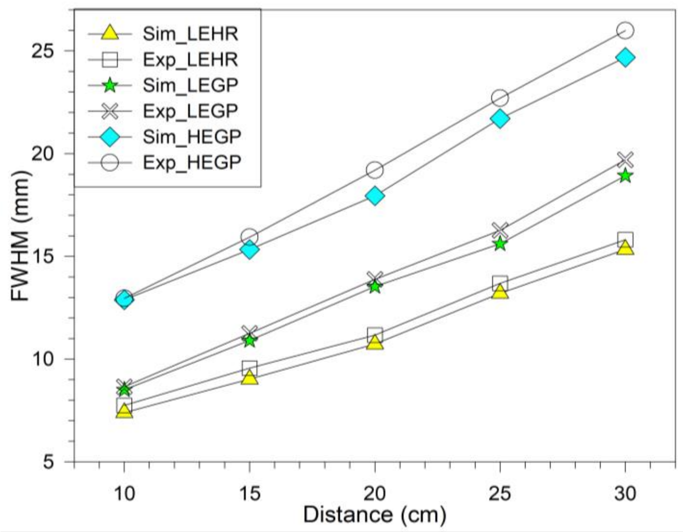

Figure 27. Experimental and simulation values of FWHM

3.1.2. Optimization

The planar sensitivity values of SPECT scanners modeled with various collimators (LEHR, LEGP, and HEGP) at different diameters and hole lengths are shown in Figure 28, Figure 29, and Figure 30. These figures show that sensitivity values are enhancing with increasing diameters, while these values deteriorate with increasing hole lengths for the models with LEHR, LEGP, and HEGP collimators.

Adjusting the hole lengths from 35 mm to 37 mm results in sensitivity decreases of 11.10%-11.30% for the LEHR collimator at 1.48 mm, 1.50 mm, and 1.52 mm diameters. When the LEHR collimator is compared to the LEGP collimator with 1.88 mm, 1.90 mm, and 1.92 mm diameters, sensitivity values ranging from 11.13% to 11.15% were obtained for the identical variation in the collimator's hole length. Conversely, the sensitivity values are reduced from 12.01% to 12.16% as a result of an increase in the hole lengths from 55 mm to 57 mm for the HEGP collimator with 3.38 mm, 3.4 mm, and 3.42 mm diameters. Based on the diameter augmentation, the sensitivity enhancement values for the LEHR, LEGP, and HEGP collimators are changing from 1.60% to 6.30%, 2.20% to 4.80%, and 1.90% to 4.10%, respectively.

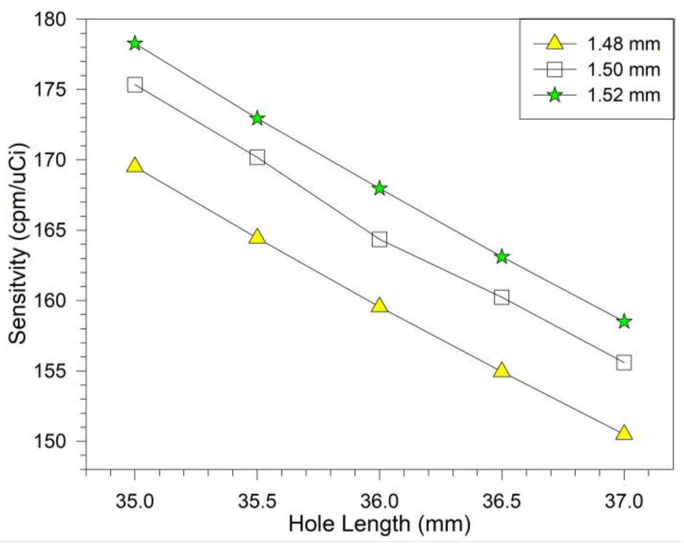

Figure 28. Sensitivity values for the SPECT using LEHR collimators

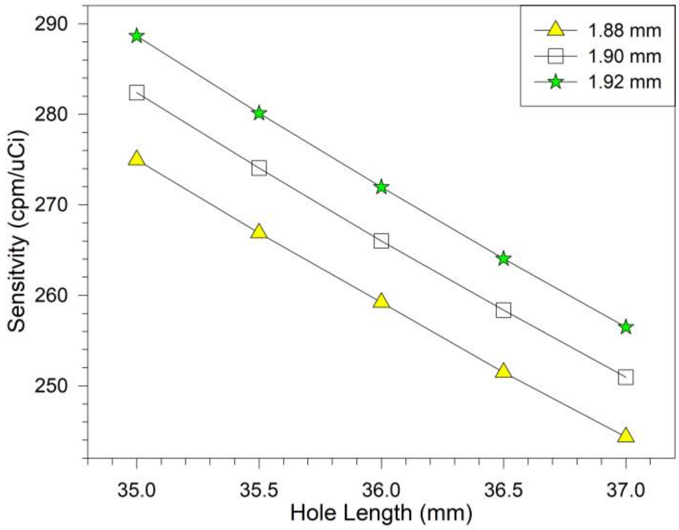

Figure 29. Sensitivity values for the SPECT using LEGP collimators

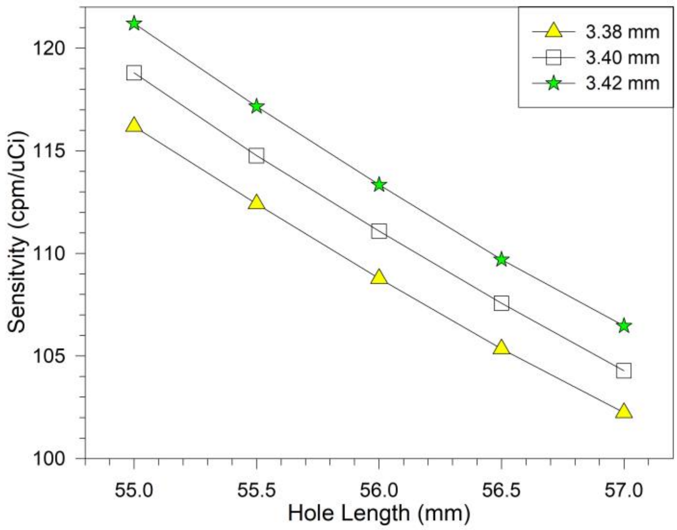

Figure 30. Sensitivity values for the SPECT using HEGP collimators

Figure 31, Figure 32, and Figure 33 present the FWHM values of SPECT scanners modeled with different collimators (LEHR, LEGP, and HEGP) over various diameters and hole lengths. The data indicate that FWHM values deteriorate as diameters increase, whereas these values improve with longer hole lengths for the models utilizing LEHR, LEGP, and HEGP collimators. In this regard, the enhancements in FWHM values are observed to range from 1.11% to 2.22% for the LEHR collimator, from 4.03% to 5.10% for the LEGP collimator, and from 2.43% to 3.97% for the HEGP collimator. With increasing diameter, FWHM values degrade from 6.60% to 8.30%, 1.70% to 6.20%, and from 1.4% to 3.5% for LEHR, LEGP, and HEGP collimators, respectively.

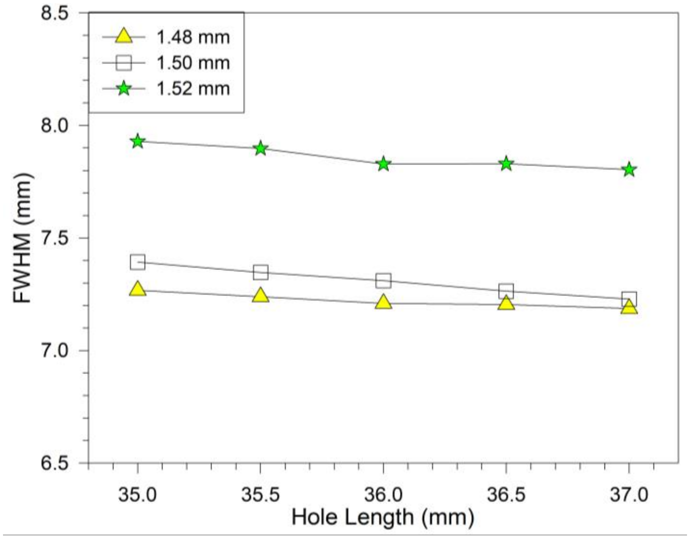

Figure 31. FWHM values for the SPECT model with LEHR collimators

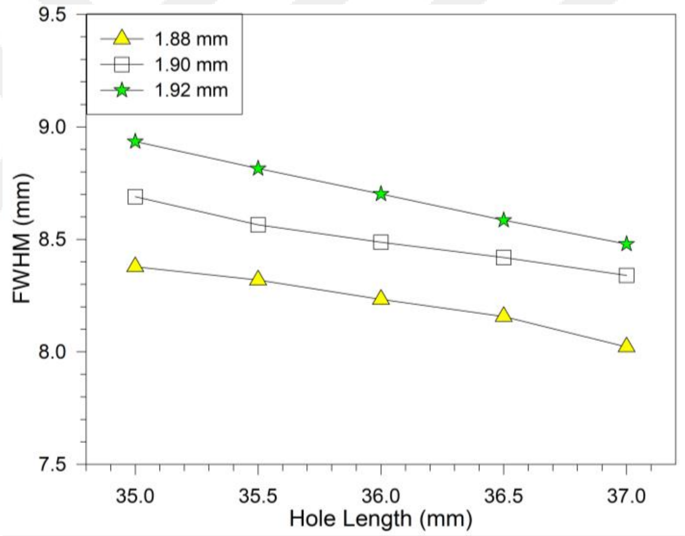

Figure 32. FWHM values for the SPECT model with LEGP collimators

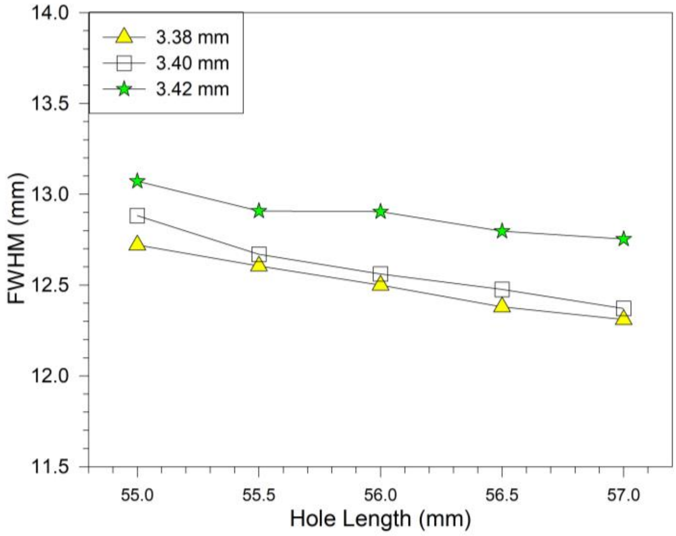

Figure 33. FWHM values for the SPECT model with HEGP collimators

It is seen that the collimator hole length expansion affects the FWHM and sensitivity. The enhancement in FWHM and loss of sensitivity arise from the augmented absorption of scattered gamma rays by the collimator. This phenomenon results in a decrease in the number of scattering events across all collimators, as demonstrated in Figure 34, Figure 35, and Figure 36.

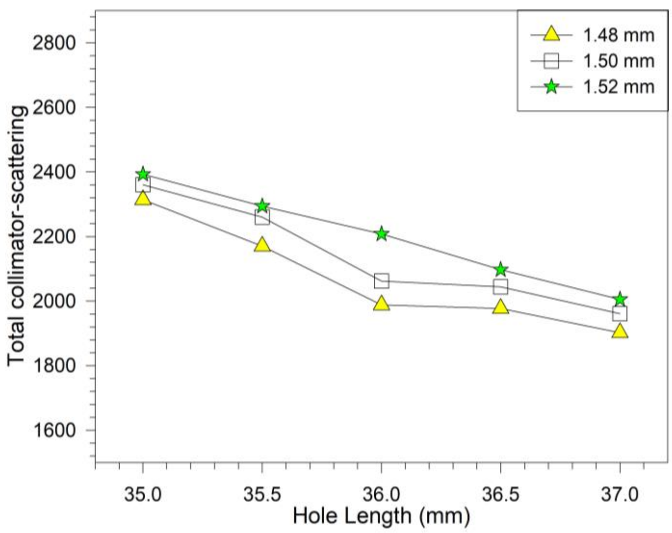

Figure 34. The scattering count number for the SPECT model with LEHR collimators

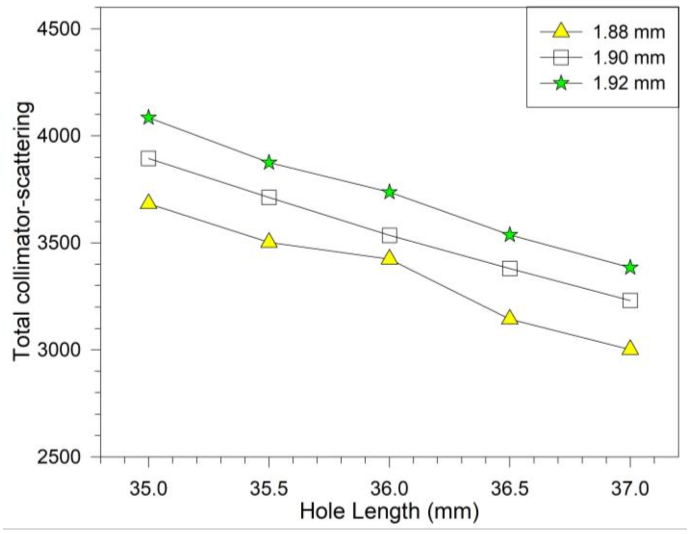

Figure 35. The scattering count number for the SPECT model with LEGP collimators

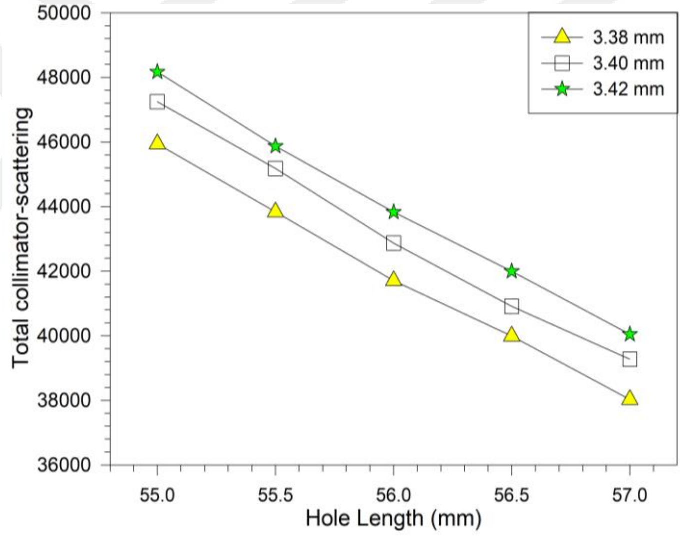

Figure 36. The scattering count number for the SPECT model with HEGP collimators

3.2. Intrinsic Performance Parameters for SPECT

3.2.1. Intrinsic Spatial Resolution

The images of quadrant bar phantoms obtained through experimental and simulation evaluations of intrinsic spatial resolution for the NaI(TI) crystal are illustrated in Figure 37. Additionally, the images generated by the simulation model of a SPECT scan with vari ous scintillation crystals are represented in Figure 38. On the quadrant bar phantom images in Figure 37, and Figure 38, the digits 1 through 4 stand for 2 mm, 2.5 mm, 3 mm, and 3.5

mm lead strips, respectively. Figure 37 and Figure 38 illustrate that the minimum resolvable bar pattern in the experimental image measures 2.5 mm in width, while the simulated SPECT scan model featuring NaI(TI) crystal and other crystal types achieves a minimum resolvable bar pattern of 2 mm in width.

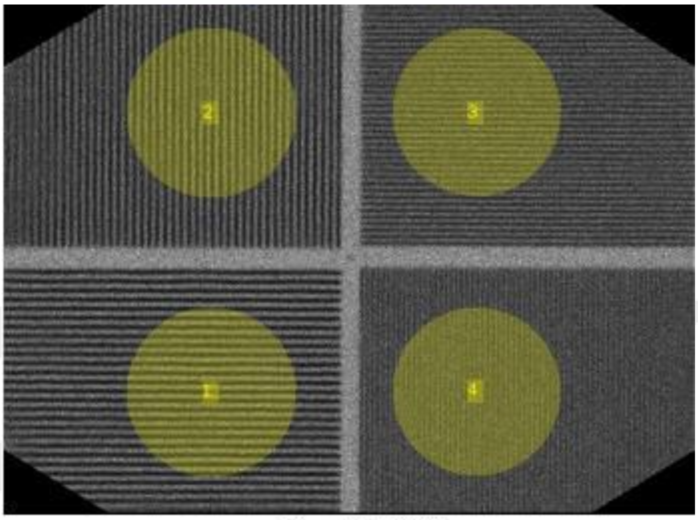

Exp NaI(TI)

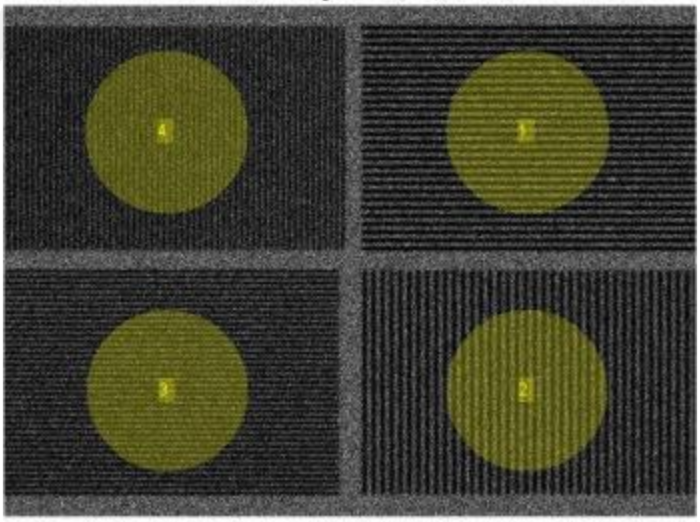

Sim NaI(TI)

Figure 37. Images of the quadrant bar phantom for the SPECT scanner at 140.5 keV energy

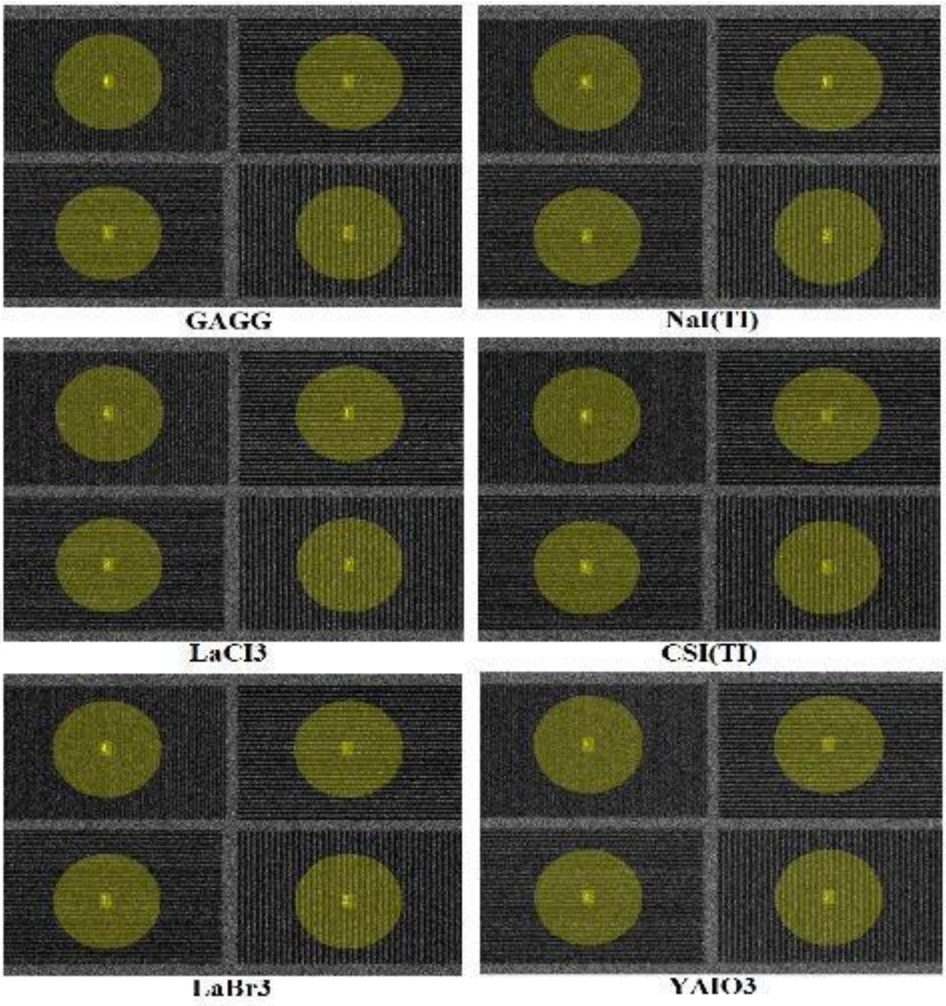

Figure 38. Images of the quadrant bar phantom for the SPECT scanner model with various types of crystals at 140.5 keV energy

This aspect is distinctly evident in the MTF data for the quadrant bar phantom patterns seen in Figure 39. The experimental SPECT scanner shows a negligible reaction to the bar pattern with a spatial bar frequency of 2.5 lp/cm, but it demonstrates an adequate response to the bar pattern with a spatial bar frequency of 2 lp/cm. The nearly perfect simulation setup, compared to real-world testing conditions, explains the different responses for various spatial frequencies. Conversely, one observes minor variations in the MTF values among the simulated SPECT scanner models utilizing NaI(TI), GAGG, CsI(TI), $LaBr_3$, and $LaCI_3$ crystals, which can be attributed to the distinct characteristics inherent to each crystal type. In contrast, the $YAIO_3$ crystal simulated SPECT scanner model's MTF values are noticeably lower than those of the other simulation models. This is because of the physical properties of this crystal, like low scintillation light yields.

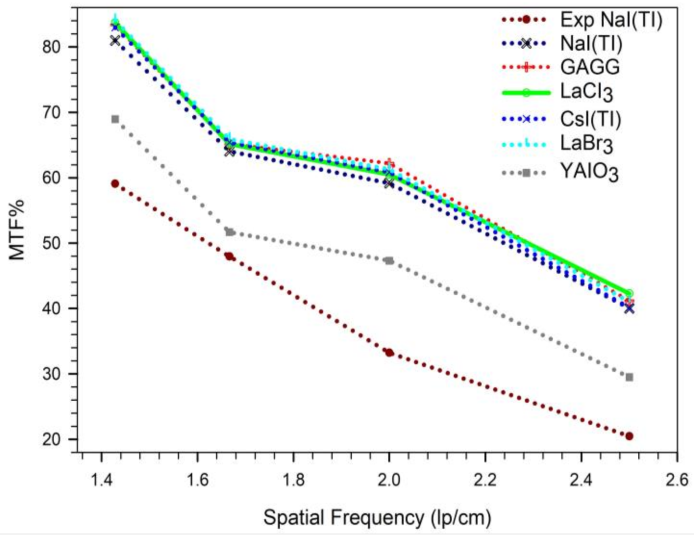

Figure 39. MTF values for the SPECT scanner model with various crystals using a quadrant bar phantom

Figure 40 and Figure 41 show the picture and image profile peaks for the lead block slit that were acquired from the SPECT scanner model utilizing the previously specified crystals at thicknesses of 12.7 mm and 15.8 mm using the ^{131}I (364.5 keV) isotope. The slit images acquired from the SPECT scanner, modeled with the crystals GAGG, NaI(TI), and $LaCI_3$ show sharpness with increasing counts, as seen in Figure 40(a); this is particularly noticeable in Figure 40(b). Blurriness is observed in the slit images of models with $LaBr_3$ and CsI(TI) crystals at low count levels. The decreased signal-to-noise ratio caused by intrinsic background radiation in the $LaBr_3$ crystal results in blurred slit images, whereas the slow decay time and intrinsic background radiation create a similar influence on the CsI(TI) crystal (Alzimami et al., 2008; Panwar et al., 2020). Especially for the model simulated using the $YAIO_3$ crystal, which has a long decay time and a low light output, the distortion at the slit images is much greater. These factors affect energy resolution by reducing the number of rejected scattering photons. Low effective atomic numbers are another factor that affects the detection number of photoelectric effects and, therefore, their effectiveness.

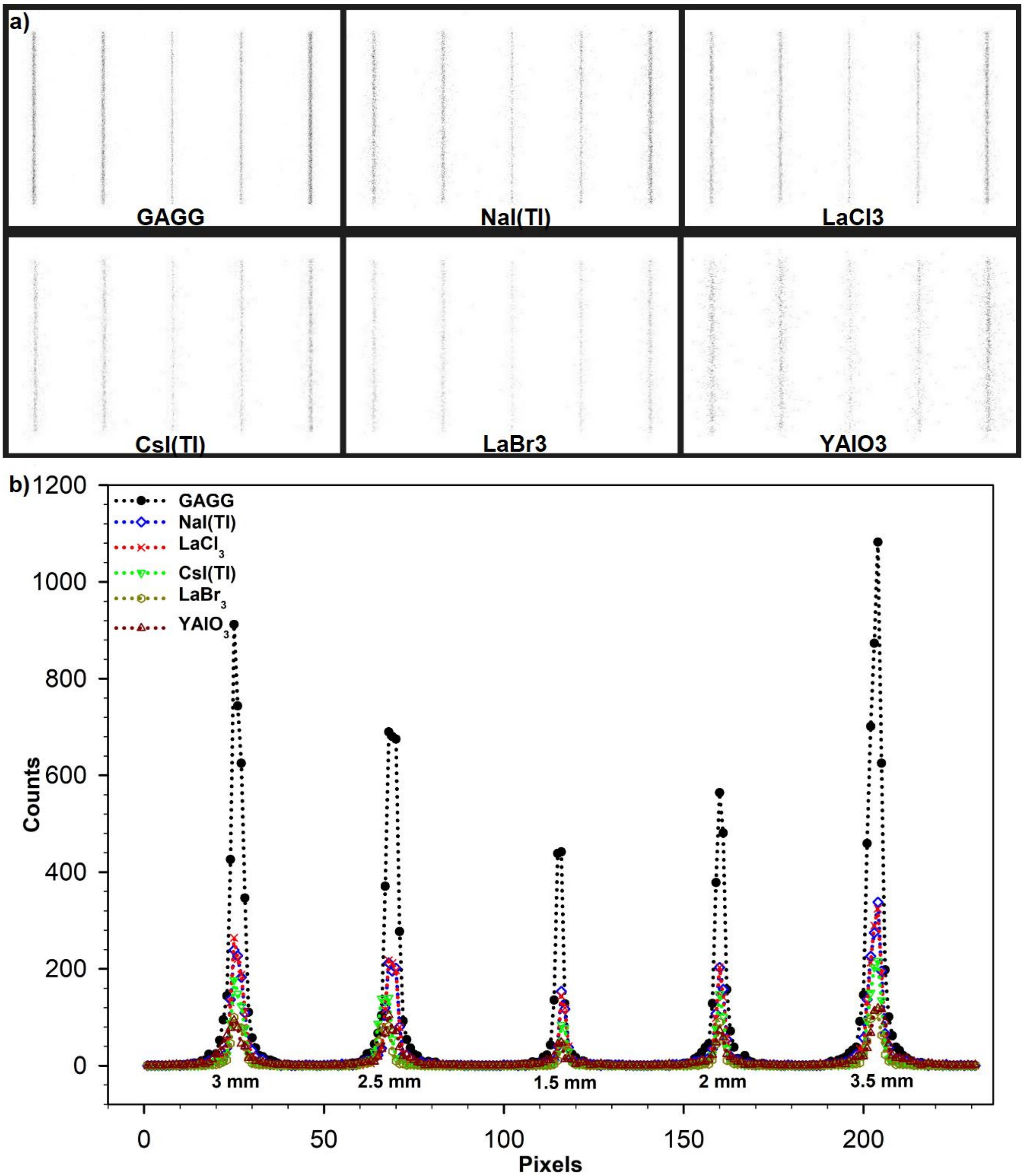

Figure 40. (a) Slit images and (b) Image profile peaks of the lead block for the SPECT models with various crystals at a 12.7 mm thickness

The distortion in the slit photos for NaI(TI), GAGG, CsI(TI), $LaCl_3$, and $YAlO_3$ crystals seen in Figure 41(a) results from an augmentation in the quantity of scattering photons and a diminution in unscattered photons as the crystal volume increases; this is evident in Figure 41(b). The slit images acquired from the SPECT scanner model using the $LaBr_3$ crystal exhibit diminished clarity relative to those generated from the SPECT scanner model using the 12.7 mm thick $LaBr_3$ crystal. This occurs due to the increasing probability of the Compton scattering effect as crystal thickness grows, as opposed to the photon electric effect (Saha, 2012).

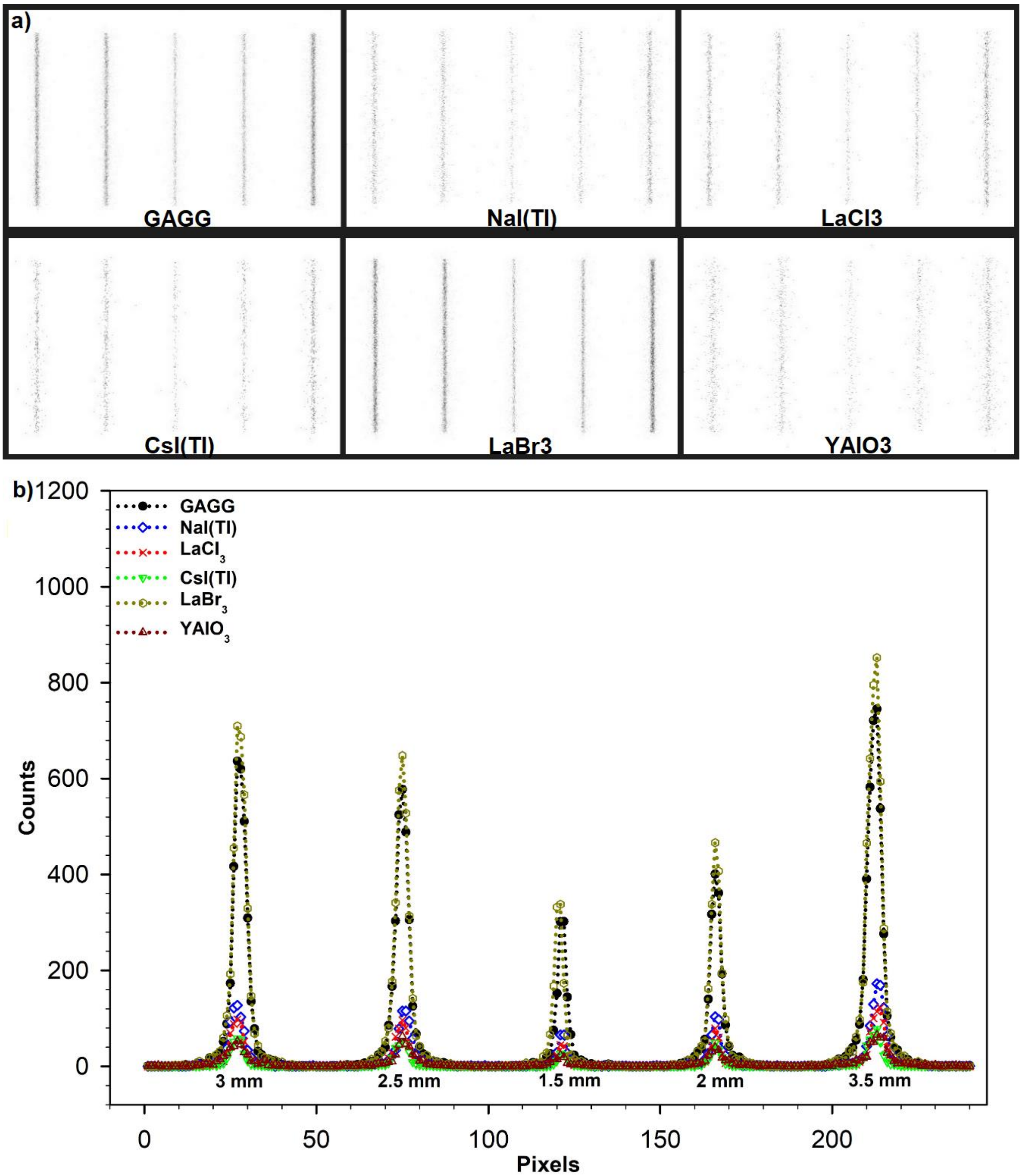

Figure 41. (a) Slit images and (b) Image profile peaks of the lead block for the SPECT models with various crystals at a 15.8 mm thickness

Table 5 shows the difference between the slit widths and the FWHM values, estimated with 12.7 mm-thick crystals, which range from 0.2 mm to 1.38 mm. Whereas these differences range from 1.38 mm to 2.94 mm for the $YAIO_3$ crystal. The match in intrinsic spatial resolution (FWHM) values between high-efficiency GAGG and $LaCl_3$ crystals and the NaI(TI) crystal decreases acquisition time during imaging, hence decreasing the quantity of radioisotope administered to the patient. When compared to the actual slit widths, the FWHM values of a 3.5 mm slit were evaluated with more accuracy than those of other slit widths, with a variance of 0.31 mm to 0.49 mm. The FWHM values varied from 1 mm to 2.01 mm with 15.8 mm thick crystals; however, they exceeded 3 mm with $LaBr_3$ and $YAIO_3$ crystals.

Table 5. Intrinsic spatial resolution of difference scintillation crystals at 365 keV

Slits Width (mm)	Crystal thicknesses (mm)	GAGG	NaI(TI)	$LaCI_3$	CsI(TI)	$LaBr_3$	$YAIO_3$
1.5		2.18 ± 0.09	2.04 ± 0.08	2.07 ± 0.08	2.27 ± 0.09	2.21 ± 0.11	2.82 ± 0.19
2.0		2.92 ± 0.09	2.64 ± 0.07	2.55 ± 0.07	2.52 ± 0.06	2.20 ± 0.06	3.48 ± 0.15
2.5	12.7	3.71 ± 0.08	3.79 ± 0.08	3.67 ± 0.07	3.88 ± 0.07	3.86 ± 0.08	4.74 ± 0.13
3.0		3.76 ± 0.07	3.92 ± 0.07	3.79 ± 0.07	3.75 ± 0.06	3.73 ± 0.07	5.94 ± 0.16
3.5		3.99 ± 0.06	4.03 ± 0.06	3.81 ± 0.05	3.83 ± 0.05	3.97 ± 0.06	5.01 ± 0.10
1.5		3.12 ± 0.08	2.79 ± 0.09	3.12 ± 0.11	3.21 ± 0.14	3.04 ± 0.08	4.69 ± 0.37
2.0		3.69 ± 0.07	3.16 ± 0.07	3.00 ± 0.07	3.31 ± 0.08	3.54 ± 0.07	5.30 ± 0.23
2.5	15.8	4.33 ± 0.05	4.44 ± 0.07	4.35 ± 0.07	4.51 ± 0.08	4.23 ± 0.05	5.47 ± 0.15
3.0		4.32 ± 0.04	4.66 ± 0.06	4.37 ± 0.06	4.17 ± 0.07	4.27 ± 0.06	6.88 ± 0.20
3.5		4.63 ± 0.04	4.56 ± 0.05	4.65 ± 0.05	4.56 ± 0.06	4.57 ± 0.04	6.06 ± 0.14

3.2.2. Intrinsic Energy Resolution

The measured intrinsic energy resolution values for both experimental and simulation models are presented in Table 6. The variation range of intrinsic energy resolution parameters for the SPECT heads (detector 1 and detector 2) and its simulation model (9.5 mm-thick NaI(TI) crystal) is 0.029%–0.199% at 140.5 keV and 0.216%–0.286% at 364.5 keV, respectively. The observed improvement in intrinsic energy resolution parameters for detectors 1 and 2, as the energy transitions from 140.6 keV to 364.5 keV, was quantified at 1.12% and 1.36%, respectively. In contrast, the enhancement simulated value was 1.61% when the energy was changed, relative to the simulation model, with a 9.5 mm-thick NaI(TI) crystal. The intrinsic energy resolution values at 140.5 keV for the SPECT scanner, simulated with various crystals (GAGG, $LaCl_3$, CsI(TI), $LaBr_3$, and $YAlO_3$) at a thickness of 9.5 mm, range from 0.001% to 0.044%, in comparison to the NaI(TI) crystal's SPECT scanner model. In a comparable instance, but for the 364.5 keV energy, the intrinsic energy resolution values range from 0.018% to 0.04%. At 364.5 keV energy, when the crystals' thicknesses were increased from 12.7 mm to 15.8 mm in the simulated SPECT scanner models, a small change in this value between 0.002% and 0.021% was noticed.

Table 6. Intrinsic energy resolution of different scintillation crystals at 140 keV and 365 keV

		Crystal thicknesses			
		9.5 mm at 140 keV	9.5 mm at 365 keV	12.7 mm at 365 keV	15.8 mm at 365 keV
Detector1	Exp%	9.89±0.18			
Detector2		10.06±0.19			
Detector1			8.767±0.5		
Detector2			8.697±0.48		
GAGG	Sim%	10.049±0.0058	8.518±0.019	8.469±0.0129	8.448±0.0064
NaI(TI)		10.089±0.006	8.481± 0.019	8.487±0.0193	8.477± 0.013
$LaCI_3$		10.088±0.006	8.514±0.019	8.496± 0.006	8.489± 0.013
CSI(TI)		10.088±0.005	8.509± 0.006	8.489± 0.013	8.487± 0.013
$LaBr_3$		10.045±0.006	8.499± 0.013	8.494± 0.013	8.481± 0.013
$YAIO_3$		10.103±0.007	8.521± 0.026	8.539±0.0193	8.523± 0.019

3.2.3. Intrinsic Uniformity

The results of the DU and IU intrinsic uniformity assessments using the experimental and SPECT scan simulation models are shown in Table 7. The differences between the simulation-determined DU and IU intrinsic uniformity values of the SPECT utilising various crystals and the values from the experimental measurements for detector 1 range from 0.401% to 0.562% for UFOV and 0.247% to 0.358% for CFOV. At detector 2, however, these values range from 0.118% to 0.191% for CFOV and 0.136% to 0.272% for UFOV in relation to DUs and IUs, respectively. The parameter values for the experiment and simulation are within the acceptable limit of intrinsic uniformity (Cherry et al., 2003; Saha, 2012; Zanzonico, 2008).

Table 7. Experimental and simulation values for uniformity

		DU%		IU%	
		UFOV	CFOV	UFOV	CFOV
Detector 1	Exp	2.278	2.278	3.482	2.952
Detector 2		2.407	2.407	4.180	3.501
GAGG	Sim	2.831	2.632	4.270	4.012
Na(TI)		2.679	2.525	4.044	3.310
LaCl3		2.786	2.786	4.204	3.627
CsI(TI)		2.617	2.617	4.311	3.737
$LaBr_3$		2.764	2.764	4.271	3.742
$YAlO_3$		2.660	2.660	3.926	3.371

3.3. Performance Parameters for PET

3.3.1. Sensitivity

Figure 42 illustrates the experimentally measured sensitivity values for the PET scanner using tubes with different thicknesses, both at the center of the transaxial FOV and 10 cm offset from the transaxial FOV. Relative to thicknesses varying from 1.25 mm to 6.25 mm, these values range from 6883 MBq/mL to 4795 MBq/mL for the measurements at the center of the transaxial FOV, whereas for the measurements at the 10 cm offset, they range from 4686 MBq/mL to 5183 MBq/mL. The sensitivity value at the 1.25 mm thickness (the first sleeve) is within acceptable values, differing inversely by 13.9% from the manufacturer's value.

The sensitivity parameter values that were estimated for the PET scanner model are shown in Figure 43. The variation in simulated sensitivity values for the two assessment cases (the center and 10 cm offset) ranges from 861 MBq/mL to 688 MBq/mL and from 822 MBq/mL to 765 MBq/mL, respectively, as the thicknesses vary. In the center of the transaxial FOV, the sensitivity value for the PET scanner model differs from the manufacturer's value by 7.6% at the 1.25 mm thickness, while the difference is 25.1% from the experimentally measured value. There is a satisfactory agreement between simulated and manufacturer's sensitivity values.

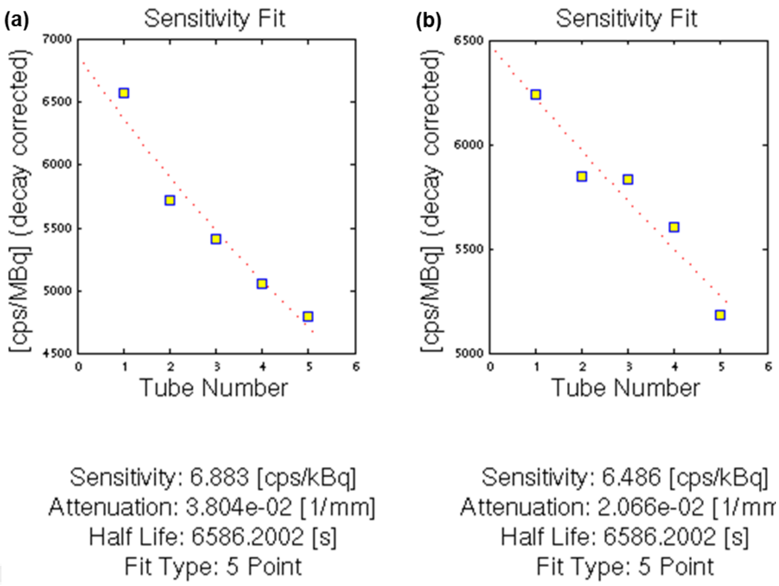

Figure 42. Sensitivity values for the PET scanner (a) at the center of the transaxial FOV and (b) at 10 cm offset from the transaxial FOV

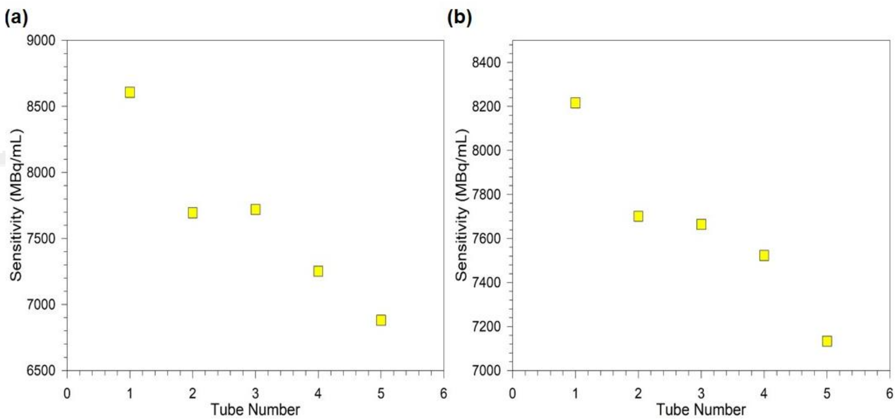

Figure 43. Sensitivity values for the PET scanner model(a) at the center of the transaxial FOV and (b) at 10 cm offset from the transaxial FOV

3.3.2. Count Performance

Experimental and simulation evaluations of prompt events (true, random, and scattered), as well as the noisy equivalent ratio (NEC) and scattering fraction, are shown in Figure 44 and Figure 45 as a function of activity concentrations. The experimental true rate is 144 kcps at a concentration of 13.3 kBq/mL. In comparison, at the same activity concentration, the true rates are 181 kcps and 120 kBq/mL according to simulation and manufacturer's data. Generally, there is acceptable agreement in prompt events between experimental and simulation assessments at the low activity concentration. For example, the true event values decline to 38 kcps and 47 kcps at the 2 kBq/mL activity concentration for both the experimental and simulation measurements, respectively. On the other hand, the NECR values derived from experimental and simulation assessments at 8.8 kBq/mL are 38.63 kcps and 36 kcps, while the manufacturer's guideline is 38 kcps at 9 kBq/mL.

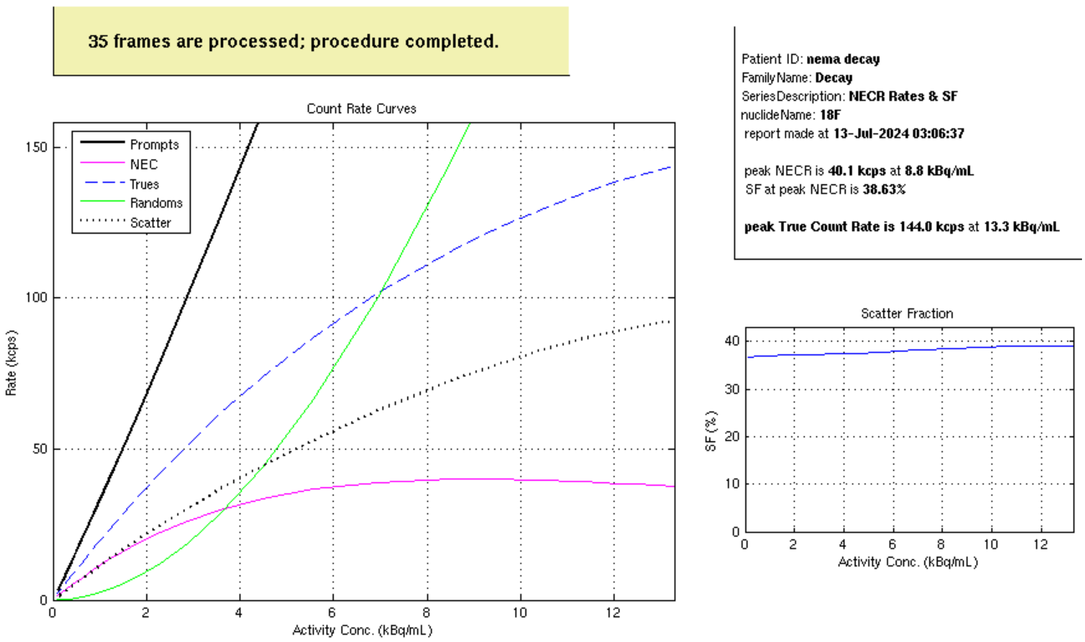

Figure 44. Experimental count rate performance

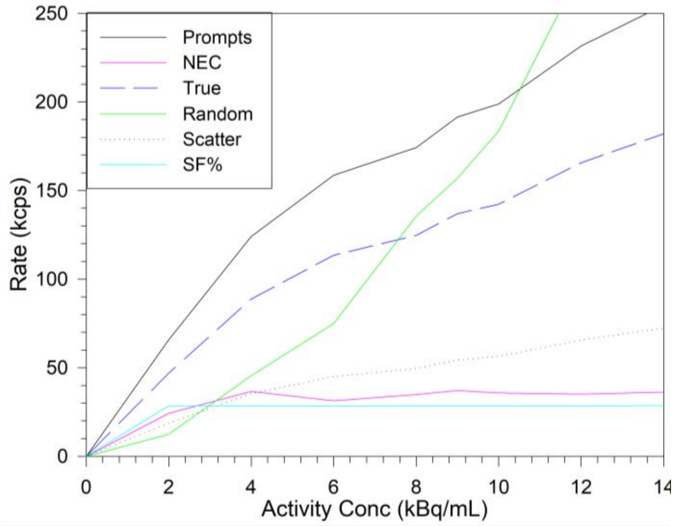

Figure 45. Simulation count rate performance

4. CONCLUSION

GATE 9.0 provided accurate simulation codes for both the dual-head Mediso Any Scan S SPECT system at SBÜ Trabzon Kanuni Education and Research Hospital and the GE Discovery-IQ PET imaging system at KTU Farabi Hospital International, to evaluate performance parameters. The developed codes achieved accurate simulation values for the predicted performance parameters of the SPECT and PET. In this regard, precise assessment values of both external performance factors at various distances and intrinsic factors at a 5 ≥ FOV distance for the SPECT scanner were obtained following NEMA quality control standards.

The collimator optimization results indicate that the LEHR collimator's optimal dimensions are 1.48 mm in diameter and 35.5 mm hole length. The specifications for the LEGP collimator were a 1.88 mm diameter and a 35 mm hole length, while the HEGP collimator had a 3.38 mm diameter and a 56 mm hole length.

Furthermore, precise values for the intrinsic performance parameters (spatial resolution, intrinsic energy resolution, and uniformity) were achieved for the SPECT scanner, which was tested using both original and different scintillation crystals. This indicates that there are minor discrepancies in the intrinsic performance parameters of GAGG, NaI(TI), $LaBr_3$, and $LaCI_3$ crystals when measured at a thickness of 9.5 mm. The FWHM values for the SPECT scan simulation models of distinct crystals (GAGG, NaI(TI), $LaBr_3$, and $LaCI_3$) with a thickness of 12.7 mm at 364.5 keV energy are better than the FWHM values for crystals with a thickness of 15.8 mm at the same energy value. The optimal thickness for scintillation crystals suitable for 364.5 keV is determined to be 12.7 mm. GAGG, $LaBr_3$, and $LaCl_3$ crystals present promising alternatives to NaI(TI) crystal at dimensions of 9.5 mm and 12.7 mm.

On the other hand, the prepared phantoms used to estimate sensitivity and count performance parameters for the PET scanner yield acceptable results. The simulated sensitivity and count performance parameters agree well with the manufactured results. In contrast, the simulated parameters align more closely with the experimental results at low activity concentrations for the count performance parameters.

5. RECOMMENDATIONS

It is seen that the GATE platform accurately simulates the SPECT device's components, which are effective on the image quality parameters. In this context, depending on the results of the intrinsic and extrinsic quality control tests for the SPECT device in this thesis, the collimator optimization for the selected scintillation crystals can possible to investigated. In addition, the converging and diverging collimators, depending on the FOV for the Mediso Any Scan S SPECT device, are possible to be designed.

Even though the simulation and experimental results of the long-distance intrinsic tests, conducted at the same detection numbers, exhibit acceptable agreement, the number of counts that were obtained from the experimental image's DICOM is higher in comparison with the simulated one. In this regard, the detection count numbers obtained from simulation tests using GATE at the mentioned conditions can be investigated.

6. REFERENCES

Abbaspour, S., Tanha, K., Mahmoudian, B., Assadi, M., & Islamian, J. P. (2018). A Monte Carlo study on the performance evaluation of a parallel hole collimator for a HiReSPECT: A dedicated small-animal SPECT. Applied Radiation and Isotopes, 139, 53-60.

Abi-Akl, M., Dadgar, M., Toufique, Y., Bouhali, O., & Vandenberghe, S. (2023). Monte Carlo simulation of the system performance of a long axial field-of-view PET based on monolithic LYSO detectors. EJNMMI Phys, 10(1), 37. doi: 10.1186/s40658-023-00559-2

Alzimami, K., Abuelhia, E., Podolyak, Z., Ioannou, A., & Spyrou, N. M. (2008). Characterization of LaBr3: Ce and LaCl3: Ce scintillators for gamma-ray spectroscopy. Journal of Radioanalytical and Nuclear Chemistry, 278(3), 755-759.

Alauddin, M. M. (2011). Positron Emission Tomography (PET) imaging with 18F-based radiotracers. American Journal of Nuclear Medicine and Molecular Imaging, 2(1), 55–76.

Apostolakis, J. (2007). An Overview of the Geant4 Toolkit. AIP Conference Proceedings, 896.

Arce, P., Bolst, D., Bordage, M. C., Brown, J., Cirrone, P., Cortés-Giraldo, M. A., . . . Dondero, P. (2021). Report on G4-Med, a Geant4 benchmarking system for medical physics applications developed by the Geant4 Medical Simulation Benchmarking Group. Medical Physics, 48(1), 19-56.

Arce, P., Bolst, D., Bordage, M. C., Brown, J. M. C., Cirrone, P., Cortés-Giraldo, M. A., . . . Wright, D. H. (2021). Report on G4-Med, a Geant4 benchmarking system for medical physics applications developed by the Geant4 Medical Simulation Benchmarking Group. Med Phys, 48(1), 19-56.

Ashoor, M., & Khorshidi, A. (2023). Modeling modulation transfer function based on analytical functions in imaging systems. The European Physical Journal Plus, 138(3), 249.

Asmi, H., Bentayeb, F., Bouzekraoui, Y., Bonutti, F., & Douama, S. (2020). Energy window and collimator optimization in Lutetium-177 single-photon emission computed tomography imaging using monte carlo simulation. Indian Journal of Nuclear Medicine, 35(1), 36-39.

Assié, K., Breton, V., Buvat, I., Comtat, C., Jan, S., Krieguer, M., . . . Walle, R. V. d. (2004). Monte Carlo simulation in PET and SPECT instrumentation using OPENGATE. Nuclear Instruments and Methods in Physics Research Section A: Accelerators, Spectrometers, Detectors and Associated Equipment, 527(1), 180-189.

Assié, K., Gardin, I., Vera, P., & Buvat, I. (2005). Validation of the Monte Carlo simulator OPENGATE for indium-111 imaging. Physics in Medicine & Biology, 50(13), 3113.

Bailey, D., Humm, J., Todd-Pokropek, A., & Aswegen, A. v. (2014). Nuclear Medicine Physics: A Handbook for Teachers and Students. Endorsed by: American Association of Physicists in Medicine (AAPM), Asia–Oceania Federation of Organizations for Medical Physics (AFOMP), Australasian College of Physical Scientists and Engineers in Medicine (ACPSEM), European Federation of Organisations for Medical Physics (EFOMP), Federation of African Medical Physics Organisations (FAMPO), World Federation of Nuclear Medicine and Biology (WFNMB).

Bailey, D. L., Townsend, D. W., Valk, P. E., & Maisey, M. N. (2005). Positron Emission Tomography: Basic Sciences: Springer London.

Basu, S., Kwee, T. C., Surti, S., Akin, E. A., Yoo, D., & Alavi, A. (2011). Fundamentals of PET and PET/CT imaging. Ann N Y Acad Sci, 1228, 1-18.

Beijst, C., Elschot, M., Viergever, M. A., & de Jong, H. W. (2015). A parallel-cone collimator for high-energy SPECT. J Nucl Med, 56(3), 476-482.

Bergmann, H., Sokole, E., MC, C. T., Dondi, M., & Fraxedas, R. (2009). Quality assurance for SPECT systems. Austria: IAEA.

Bhatia, B. S., Bugby, S. L., Lees, J. E., & Perkins, A. C. (2015). A scheme for assessing the performance characteristics of small field-of-view gamma cameras. Phys Med, 31(1), 98-103.

Buvat, I., & Castiglioni, I. (2002). Monte Carlo simulations in SPET and PET. Q J Nucl Med, 46(1), 48-61.

Buvat, I., & Lazaro, D. (2006). Monte Carlo simulations in emission tomography and OPENGATE: An overview. Nuclear Instruments and Methods in Physics Research Section A: Accelerators, Spectrometers, Detectors and Associated Equipment, 569, 323-329.

Cherry, S., Sorenson, J. A., & Phelps, M. (2003). Physics in Nuclear Medicine (Vol. 31, pp. 523).

Conti, M., & Eriksson, L. (2016). Physics of pure and non-pure positron emitters for PET: a review and a discussion. EJNMMI Physics, 3(1).

Crișan, G., Moldovean-Cioroianu, N. S., Timaru, D.-G., Andrieș, G., Căinap, C., & Chiș, V. (2022). Radiopharmaceuticals for PET and SPECT Imaging: A Literature Review over the Last Decade. International Journal of Molecular Sciences, 23(9), 5023.

Dahlbom, M. (2017). Physics of PET and SPECT Imaging: CRC Press.

Desmonts, C., Bouthiba, M. A., Enilorac, B., Nganoa, C., Agostini, D., & Aide, N. (2020). Evaluation of a new multipurpose whole-body CzT-based camera: comparison with a dual-head Anger camera and first clinical images. EJNMMI Phys, 7(1), 18.

Dorenbos, P., Haas, J. T. M. d., & Eijk, C. W. E. v. (1995). Non-proportionality in the scintillation response and the energy resolution obtainable with scintillation crystals. IEEE Transactions on Nuclear Science, 42(6), 2190-2202.

Elkamhawy, A. A., Rothenbach, J. R., Damaraju, S., & Badruddin, S. M. (2000). Intrinsic Uniformity and Relative Sensitivity Quality Control Tests for Single-Head Gamma Cameras. J Nucl Med Technol, 28(4), 252-256.

FAMJM, M., & MJG, M. (2012). Essentials of Nuclear Medicine Imaging: Expert Consult-Online and Print, 6e: Saunders, Philadelphia, PA.

Fleck, I., Titov, M., Grupen, C., & Buvat, I. (2021). Handbook of particle detection and imaging.

Fuin, N., Bousse, A., Pedemonte, S., Arridge, S., Ourselin, S., & Hutton, B. (2010). Collimator design in SPECT, an optimisation tool. Paper presented at the IEEE Nuclear Science Symposium & Medical Imaging Conference.

Gregory, R. A., Murray, I., Gear, J., Aldridge, M. D., Levine, D., Fowkes, L., . . . Flux, G. (2017). Objective comparison of lesion detectability in low and medium-energy collimator iodine-123 mIBG images using a channelized Hotelling observer. Physics in Medicine & Biology, 62(1), 17.

Grupen, C., & Buvat, I. (2011). Handbook of particle detection and imaging: Springer Science & Business Media.

Gündoğdu, E. A., Özgenç, E., Ekinci, M., Özdemir, D. İ., & Aşıkoğlu, M. (2018). Nükleer tıpta görüntüleme ve tedavide kullanılan radyofarmasötikler. Journal of Literature Pharmacy Sciences, 7(1), 24-34.

Gunter, D. (2004). Collimator Design for Nuclear Medicine (pp. 153-168).

Hacker, M., Beyer, T., Baum, R. P., Kalemis, A., Lammertsma, A. A., Lewington, V., . . . Verzijlbergen, F. (2015). Nuclear medicine innovations help (drive) healthcare (benefits). European journal of nuclear medicine and molecular imaging, 42(2), 173-175.

Hallen, P., Schug, D., & Schulz, V. (2020). Comments on the NEMA NU 4-2008 Standard on Performance Measurement of Small Animal Positron Emission Tomographs. EJNMMI physics, 7(1), 12.

Hander, T. A., Lancaster, J. L., Kopp, D. T., Lasher, J. C., Blumhardt, R., & Fox, P. T. (1997). Rapid objective measurement of gamma camera resolution using statistical moments. Med Phys, 24(2), 327-334.

Hasan, M. R., Khan, M. H. R., Rahman, M. R., Parvez, M. S., Islam, M. R., & Paul, A. K. (2017). Quality Control of Gamma Camera with SPECT Systems. International Journal of Medical Physics, Clinical Engineering and Radiation Oncology, Vol.06No.03, 8.

Hautefeuille, M., & Hernández-Cordero, J. (2021). Photomultiplier tubes. In SPIE eBooks.

Herscovitch, P. (2003). Single Photon Emission Computed Tomography (SPECT). In M. J. Aminoff & R. B. Daroff (Eds.), Encyclopedia of the Neurological Sciences (pp. 279-284). New York: Academic Press.

Herscovitch, P. (2014). Single-Photon Emission Computed Tomography (SPECT). In M. J. Aminoff & R. B. Daroff (Eds.), Encyclopedia of the Neurological Sciences (Second Edition) (pp. 173-178). Oxford: Academic Press.

Holstensson, M., Partridge, M., Buckley, S. E., & Flux, G. D. (2010). The effect of energy and source location on gamma camera intrinsic and extrinsic spatial resolution: an experimental and Monte Carlo study. Physics in Medicine & Biology, 55(6), 1735.

İnce, C., Karadeniz, Ö., Ertay, T., & Durak, H. (2021). Collimator and energy window optimization for YTTRIUM-90 bremsstrahlung SPECT imaging. Applied Radiation and Isotopes, 167, 109453.

Ivanchenko, V., Apostolakis, J., Bagulya, A., Abdelouahed, H. B., Black, R., Bogdanov, A., Burkhard, H., Chauvie, S., Cirrone, P., Cuttone, G., Depaola, G., Di Rosa, F., Elles, S., Francis, Z., Grichine, V., Gumplinger, P., Gueye, P., Incerti, S., Ivanchenko, A., … Zacharatou, C. (2011). Recent improvements in GEANT4 Electromagnetic Physics models and interfaces. Progress in Nuclear Science and Technology, 2(0), 898–903.

Jan, S., Benoit, D., Becheva, E., Carlier, T., Cassol, F., Descourt, P., Frisson, T., Grevillot, L., Guigues, L., Maigne, L., Morel, C., Perrot, Y., Rehfeld, N., Sarrut, D., Schaart, D. R., Stute, S., Pietrzyk, U., Visvikis, D., Zahra, N., & Buvat, I. (2011). OPENGATE V6: a major enhancement of the OPENGATE simulation platform enabling modelling of CT and radiotherapy. Physics in Medicine and Biology, 56(4), 881–901.

Jan, S., Santin, G., Strul, D., Staelens, S., Assié, K., Autret, D., . . . Morel, C. (2004). OPENGATE: a simulation toolkit for PET and SPECT. Phys Med Biol, 49(19), 4543-4561.

Kharfi, F. (2013). Principles and applications of nuclear medical imaging: a survey on recent developments. Imaging Radioanal. Tech. Interdiscip. Res.-Fundam. Cut. Edge Appl.

Kijewski, M. F. (2016). Chapter 32 - Positron Emission Tomography (PET) and Single-Photon Emission Computed Tomography (SPECT) Physics. In H. B. Newton (Ed.), Handbook of Neuro-Oncology Neuroimaging (Second Edition) (pp. 353-358). San Diego: Academic Press.

Kim, C., Lee, W., Melis, A., Elmughrabi, A., Lee, K., Park, C., & Yeom, J.-Y. (2021). A Review of Inorganic Scintillation Crystals for Extreme Environments. Crystals, 11(6), 669.

Kim, H. C., Kim, H.-J., Kim, K., Lee, M.-H., & Lee, Y. (2017). Comparison of Image Uniformity with Photon Counting and Conventional Scintillation Single-Photon Emission Computed Tomography System: A Monte Carlo Simulation Study. Nuclear Engineering and Technology, 49(4), 776-780.

Li, S., Zhang, Q., Xie, Z., Liu, Q., Xu, B., Yang, K., . . . Ren, Q. (2015). OPENGATE simulation of a LYSO-based SPECT imager: Validation and detector optimization. Nuclear Instruments and Methods in Physics Research Section A: Accelerators, Spectrometers, Detectors and Associated Equipment, 773, 21-26.

Loudos, G. (2007). Monte Carlo simulations in Nuclear Medicine. AIP Conference Proceedings, 958, 147-150.

Lu, L., Zhang, H., Bian, Z., Ma, J., Feng, Q., & Chen, W. (2016). Validation of a Monte Carlo simulation of the Inveon PET scanner using OPENGATE. Nuclear Instruments and Methods in Physics Research Section A: Accelerators, Spectrometers, Detectors and Associated Equipment, 828, 170-175.

MacManus, M., Nestle, U., Rosenzweig, K. E., Carrio, I., Messa, C., Belohlavek, O., . . . Schipani, S. (2009). Use of PET and PET/CT for radiation therapy planning: IAEA expert report 2006–2007. Radiotherapy and oncology, 91(1), 85-94.

Massari, R., D'Elia, A., Soluri, A., & Soluri, A. (2020). Super Spatial Resolution (SSR) method for small animal SPECT imaging: A Monte Carlo study. Nuclear Instruments and Methods in Physics Research Section A: Accelerators, Spectrometers, Detectors and Associated Equipment, 982, 164584.

Mikalsen, L. T. G., Kvassheim, M., & Stokke, C. (2023). Optimized SPECT Imaging of (224)Ra α-Particle Therapy by (212)Pb Photon Emissions. J Nucl Med, 64(7), 1131-1137.

Moore, S. C., Kouris, K., & Cullum, I. (1992). Collimator design for single photon emission tomography. Eur J Nucl Med, 19(2), 138-150.

Moslemi, V., & Ashoor, M. (2017). Design and performance evaluation of a new high energy parallel hole collimator for radioiodine planar imaging by gamma cameras: Monte Carlo simulation study. Annals of nuclear medicine, 31(4), 324-334.

Moszyński, M. (2003). Inorganic scintillation detectors in γ-ray spectrometry. Nuclear Instruments and Methods in Physics Research Section A: Accelerators, Spectrometers, Detectors and Associated Equipment, 505(1), 101-110.

Moszyński, M., Syntfeld-Każuch, A., Swiderski, L., Grodzicka, M., Iwanowska, J., Sibczyński, P., & Szczęśniak, T. (2016). Energy resolution of scintillation detectors. Nuclear Instruments and Methods in Physics Research Section A: Accelerators, Spectrometers, Detectors and Associated Equipment, 805, 25-35.

Moszyński, M., Zalipska, J., Balcerzyk, M., Kapusta, M., Mengesha, W., & Valentine, J. D. (2002). Intrinsic energy resolution of NaI(Tl)11Support for this work was provided by the Polish Committee for Scientific Research, Grant No 8 T10C 002 20. Nuclear Instruments and Methods in Physics Research Section A: Accelerators, Spectrometers, Detectors and Associated Equipment, 484(1), 259-269.

NEMA (2018). Performance measurements of gamma cameras. NEMA NU 1-2018. National Electrical Manufacturers Association.

Noori-Asl, M., & Jeddi-Dashghapou, S. (2022). Investigation of Different Components of Parallel-Hole Collimator Response to Different Radioisotope Energies Used in Nuclear Medicine Imaging. J Med Phys, 47(3), 294-300.

Nuzzo, R. L. (2019). Histograms: A useful data analysis visualization. PM&R, 11(3), 309-312.

Panwar, S., Mazumdar, I., Sariyal, R., Ranga, V., Patel, S. M., Chavan, P. B., & Gourishetty, A. K. (2020). Characterization of a Sr co-doped LaBr3:(Ce) detector for γ-ray spectroscopy. Nuclear Instruments and Methods in Physics Research Section A: Accelerators, Spectrometers, Detectors and Associated Equipment, 982, 164567.

Payolla, F. B., Massabni, A. C., & Orvig, C. (2019). Radiopharmaceuticals for diagnosis in nuclear medicine: A short review. Eclética Química, 44(3), 11-19.

Pells, S., Cullen, D. M., Deidda, D., Denis-Bacelar, A. M., Fenwick, A., Ferreira, K. M., . . . Needham, G. (2023). Quantitative validation of Monte Carlo SPECT simulation: application to a Mediso AnyScan OPENGATE simulation. EJNMMI physics, 10(1), 60.

Peterson, T. E., & Furenlid, L. R. (2011). SPECT detectors: the Anger Camera and beyond. Phys Med Biol, 56(17), R145-182.

Prekeges, J. (2013). Nuclear medicine instrumentation: Jones & Bartlett Learning Burlington, MA.

Prior, J. O., & Lecoq, P. (2012). Radiation-Based Medical Imaging Techniques: An Overview. In C. Grupen & I. Buvat (Eds.), Handbook of Particle Detection and Imaging (pp. 857-881). Berlin, Heidelberg: Springer Berlin Heidelberg.

Rasouli, M., Takavar, A., Ay, M. R., Saber, S., & Loudos, G. (2010). Effects of crystal pixel size and collimator geometry on the performance of a pixelated crystal gamma-camera using Monte Carlo simulation. J Nucl Med Technol, 38(4), 199-204.

Rault, E., Staelens, S., Van Holen, R., De Beenhouwer, J., & Vandenberghe, S. (2011). Accurate Monte Carlo modelling of the back compartments of SPECT cameras. Phys Med Biol, 56(1), 87-104.

Rezaei, H., Sheikhzadeh, P., Ghafarian, P., Zaidi, H., & Ay, M. R. (2023). Accurate modeling and performance evaluation of a total-body pet scanner using Monte Carlo simulations. Med Phys, 50(11), 6815-6827.

Robilotta, C. (2004). Emission Tomography: SPECT and PET. Computación y Sistemas, 7, 167-174.

Rong, X., & Frey, E. C. (2013). A collimator optimization method for quantitative imaging: Application to Y-90 bremsstrahlung SPECT. Medical Physics, 40(8), 082504.

Saaidi, R., Toufique, Y., Zeghari, A., Kharrim, A., & Cherkaoui El Moursli, R. (2018). OPENGATE Simulation of a Clinical PET Scanner: Influence of Windows Timing Coincidences and Dead Time on Count Rate Performance.

Sadremomtaz, A., & Telikani, Z. (2018). Capabilities of the Monte Carlo simulation codes for modeling of a small animal SPECT camera. Nuclear Medicine and Molecular Imaging, 52(4), 303-310.

Saha, G. B., & Broga, D. (2011). Basics of PET imaging: physics, chemistry, and regulations. Medical Physics-New York-Institute of Physics, 38(2), 1124.

Saha, G. B. (2012). Physics and radiobiology of nuclear medicine: Springer Science & Business Media.

Salgado, W. L., Dam, R. S. d. F., Ramos, L. L., da Silva, A. X., Conti, C. C., & Salgado, C. M. (2022). Experimental and simulated methods to characterize the response of a scintillator detector. Radiation Physics and Chemistry, 192, 109895.

Samanta, S., Jiang, J., Hamdi, M., Register, A. Z., Majewski, S., Williams, M. B., . . . Tai, Y. C. (2021). Performance comparison of a dedicated total breast PET system with a clinical whole-body PET system: a simulation study. Phys Med Biol, 66(11).

Sarrut, D., Etxebeste, A., Munoz, E., Krah, N., & Letang, J. M. (2021). Artificial intelligence for Monte Carlo simulation in medical physics. Frontiers in Physics, 9, 738112.

Sarrut, D., Arbor, N., Baudier, T., Borys, D., Etxebeste, A., Fuchs, H., Gajewski, J., Grevillot, L., Jan, S., Kagadis, G. C., Kang, H. G., Kirov, A., Kochebina, O., Krzemien, W., Lomax, A., Papadimitroulas, P., Pommranz, C., Roncali, E., Rucinski, A., … Maigne, L. (2022). The OpenGATE ecosystem for Monte Carlo simulation in medical physics. *Physics in Medicine and Biology*, *67*(18), 184001.

Schmidtlein, C. R., Kirov, A. S., Nehmeh, S. A., Erdi, Y. E., Humm, J. L., Amols, H. I., . . . Hamacher, K. A. (2006). Validation of OPENGATE Monte Carlo simulations of the GE Advance/Discovery LS PET scanners. Med Phys, 33(1), 198-208.

Sharp, P. F., Gemmell, H. G., Murray, A. D., & Sharp, P. F. (2005). Practical nuclear medicine (Vol. 26): Springer.

Sheen, H., Im, K., Choi, Y., Shin, H., Han, Y., Chung, K., . . . Ahn, S. H. (2015). OPENGATE Monte Carlo simulation of GE Discovery 600 and a uniformity phantom. Journal of the Korean Physical Society, 65, 1802-1808.

Sheikhzadeh, P., Sabet, H., Ghadiri, H., Geramifar, P., Mahani, H., Ghafarian, P., & Ay, M. R. (2017). Development and validation of an accurate OPENGATE model for NeuroPET scanner. Phys Med, 40, 59-65.

Shukla, A. K., & Kumar, U. (2006). Positron emission tomography: An overview. J Med Phys, 31(1), 13-21.

Soni, P. S. (1992). Quality control of imaging devices (No. NMS--1, pp. 49-87).

Strugari, M. E., DeBay, D. R., Beyea, S. D., & Brewer, K. D. (2023). NEMA NU 1-2018 performance characterization and Monte Carlo model validation of the Cubresa Spark SiPM-based preclinical SPECT scanner. EJNMMI Phys, 10(1), 35.

Taherparvar, P., & Sadremomtaz, A. (2018). Development of OPENGATE Monte Carlo simulation for a CsI pixelated gamma camera dedicated to high resolution animal SPECT. Australasian Physical & Engineering Sciences in Medicine, 41(1), 31-39.

URL-1.(2025, June 15). OpenGATE Collaboration: http://www.opengatecollaboration.org

Uslu Aynur, H., Bayram, T., Hayder, A., & Gedik, S. (2025). Investigation of the effect of crystal dead layer on system performance in Single Photon Emission Computed Tomography: A Monte Carlo simulation study. Radiation Measurements, 181, 107363.

Van Audenhaege, K., Van Holen, R., Vandenberghe, S., Vanhove, C., Metzler, S. D., & Moore, S. C. (2015). Review of SPECT collimator selection, optimization, and fabrication for clinical and preclinical imaging. Med Phys, 42(8), 4796-4813.

Wang, R., Zhang, D., Hu, Y., Lyu, Z., & Ma, T. (2023). High-sensitivity cardiac SPECT system design with collimator-less interspaced mosaic-patterned scintillators. Front Med (Lausanne), 10, 1145351.

Verdonck, P. (Ed.). (2008). Advances in biomedical engineering. Elsevier.

WASSERMAN, H. J. (1998). Quantification of gamma camera spatial resolution by means of bar phantom images. Nuclear Medicine Communications, 19(11), 1089-1098.

Weinmann, A. L., Hruska, C. B., & O'Connor, M. K. (2009). Design of optimal collimation for dedicated molecular breast imaging systems. Med Phys, 36(3), 845-856.

Weng, F., Bagchi, S., Zan, Y., Huang, Q., & Seo, Y. (2016). An energy-optimized collimator design for a CZT-based SPECT camera. Nucl Instrum Methods Phys Res A, 806, 330-339.

Weng, F., Bagchi, S., Zan, Y., Huang, Q., & Seo, Y. (2016). An energy-optimized collimator design for a CZT-based SPECT camera. Nuclear Instruments and Methods in Physics Research Section A: Accelerators, Spectrometers, Detectors and Associated Equipment, 806, 330-339.

Wernick, M. N., & Aarsvold, J. N. (2004). Emission tomography : the fundamentals of PET and SPECT (1st ed. ed.). Amsterdam ;: Elsevier Academic Press.

Winterhalter, C., Taylor, M., Boersma, D., Elia, A., Guatelli, S., Mackay, R., . . . Resch, A. F. (2020). Evaluation of OPENGATE-RTion (OPENGATE/Geant4) Monte Carlo simulation settings for proton pencil beam scanning quality assurance. Medical Physics, 47(11), 5817-5828.

Xu, S., Yan, Z., & Wei, Q. (2024). A Survey of Crystals for SPECT Imaging. Crystals, 14(12), 1039.

Zanzonico, P. (2008). Routine Quality Control of Clinical Nuclear Medicine Instrumentation: A Brief Review. Journal of Nuclear Medicine, 49(7), 1114-1131.

Zanzonico, P. (2013). Instrumentation. In H. W. Strauss, G. Mariani, D. Volterrani, & S. M. Larson (Eds.), Nuclear Oncology: Pathophysiology and Clinical Applications (pp. 93-120). New York, NY: Springer New York.

Zanzonico, P. (2014). Physics in Nuclear Medicine. Medical Physics, 41(3).

7. APPENDIX

Appendix 1

```
#POINT SOURCE
/gate/source/addSource Tc-99m
/gate/source/ Tc-99m /gps/particle gamma
/gate/source/ Tc-99m /setActivity  1 mCi
/gate/source/ Tc-99m /gps/energytype Mono
/gate/source/ Tc-99m /gps/monoenergy 140  keV
/gate/source/ Tc-99m /gps/type Point
/gate/source/ Tc-99m/gps/pos/centre  0.   2.15   0. m
/gate/source/ Tc-99m/gps/angtype iso

# DIGITIZER FOR SPECT DIVCE
/gate/digitizer/Singles/insert adder
/gate/digitizer/Singles/insert readout
/gate/digitizer/Singles/insert crystalblurring
/gate/digitizer/Singles/crystalblurring/setCrystalResolutionMin 0.07
/gate/digitizer/Singles/crystalblurring/setCrystalResolutionMax 0.10
/gate/digitizer/Singles/crystalblurring/setCrystalEnergyOfReference 364.5 keV
/gate/digitizer/Singles/insert spblurring
/gate/digitizer/Singles/spblurring/setSpresolution 2 mm
/gate/digitizer/Singles/insert thresholder
/gate/digitizer/Singles/thresholder/setThreshold 291.6 or 168.5  keV
/gate/digitizer/Singles/insert upholder
/gate/digitizer/Singles/upholder/setUphold 437.4 or 112.5  keV
```

Appendix 2

```
# LINE 1
/gate/world/daughters/name Phantom1
/gate/world/daughters/insert cylinder
/gate/Phantom1/geometry/setRmin 0.55 mm
/gate/Phantom1/geometry/setRmax 0.75 mm
/gate/Phantom1/geometry/setHeight 7.5 cm
/gate/Phantom1/placement/setTranslation 5. 0. 0. cm
/gate/Phantom1/setMaterial Plexiglass
/gate/Phantom1/vis/setColor blue
/gate/Phantom1/placement/setRotationAxis 0 1 0
/gate/Phantom1/placement/setRotationAngle 180 deg
# LINE 2
/gate/world/daughters/name Phantom2
/gate/world/daughters/insert cylinder
/gate/Phantom2/geometry/setRmin 0.55 mm
/gate/Phantom2/geometry/setRmax 0.75 mm
/gate/Phantom2/geometry/setHeight 7.5 cm
/gate/Phantom2/placement/setTranslation -5. 0. 0. cm
/gate/Phantom2/setMaterial Plexiglass
/gate/Phantom2/vis/setColor blue
/gate/Phantom2/placement/setRotationAxis 0 1 0
/gate/Phantom2/placement/setRotationAngle 180 deg
# LINE  3
/gate/world/daughters/name Phantom3
/gate/world/daughters/insert cylinder
/gate/Phantom3/geometry/setRmin 0.55 mm
/gate/Phantom3/geometry/setRmax 0.75 mm
/gate/Phantom3/geometry/setHeight 7.5 cm
/gate/Phantom3/placement/setTranslation 0. 0. 5. cm
/gate/Phantom3/setMaterial Plexiglass
/gate/Phantom3/vis/setColor blue
/gate/Phantom3/placement/setRotationAxis 0 1 0
/gate/Phantom3/placement/setRotationAngle 90 deg
# LINE  4
/gate/world/daughters/name Phantom4
/gate/world/daughters/insert cylinder
/gate/Phantom4/geometry/setRmin 0.55 mm
/gate/Phantom4/geometry/setRmax 0.75 mm
/gate/Phantom4/geometry/setHeight 7.5 cm
/gate/Phantom4/placement/setTranslation 0. 0. -5. cm
/gate/Phantom4/setMaterial Plexiglass
/gate/Phantom4/vis/setColor blue
/gate/Phantom4/placement/setRotationAxis 0 1 0
/gate/Phantom4/placement/setRotationAngle 90 deg
```

Appendix 3

```
/gate/world/daughters/name Phantom1
/gate/world/daughters/insert box
/gate/Phantom1/geometry/setXLength  43.2 cm
/gate/Phantom1/geometry/setYLength  8. mm
/gate/Phantom1/geometry/setZLength  58.8 cm
/gate/Phantom1/placement/setTranslation 0. 0. 0. cm
/gate/Phantom1/setMaterial Plexiglass
/gate/Phantom1/vis/setColor white
##BAR1 2.5 mm
/gate/Phantom1/daughters/name bar1
/gate/Phantom1/daughters/insert box
/gate/bar1/geometry/setXLength  2.5 mm
/gate/bar1/geometry/setYLength  3.25 mm
/gate/bar1/geometry/setZLength  26.2 cm
/gate/bar1/setMaterial Lead
/gate/bar1/placement/setTranslation  10.45  0.1975  -13.85 cm
/gate/bar1/repeaters/insert linear
/gate/bar1/linear/setRepeatNumber 39
/gate/bar1/linear/setRepeatVector  5   0. 0. mm
#AIR_HOLE1 2.5 mm
/gate/Phantom1/daughters/name AIR_hole1
/gate/Phantom1/daughters/insert box
/gate/AIR_hole1/geometry/setXLength  2.5 mm
/gate/AIR_hole1/geometry/setYLength  0.4 mm
/gate/AIR_hole1/geometry/setZLength  26.2 cm
/gate/AIR_hole1/setMaterial Air
/gate/AIR_hole1/placement/setTranslation  10.45  0.38 -13.85 cm
/gate/AIR_hole1/repeaters/insert linear
/gate/AIR_hole1/linear/setRepeatNumber 39
/gate/AIR_hole1/linear/setRepeatVector  5   0. 0. mm
#BAR2 2 mm
/gate/Phantom1/daughters/name bar2
/gate/Phantom1/daughters/insert box
/gate/bar2/geometry/setXLength  19.2 cm
/gate/bar2/geometry/setYLength  3.25 mm
/gate/bar2/geometry/setZLength   2 mm
/gate/bar2/placement/setTranslation  -10.45  0.1975 -13.5 cm
/gate/bar2/setMaterial Lead
/gate/bar2/repeaters/insert linear
/gate/bar2/linear/setRepeatNumber 66
/gate/bar2/linear/setRepeatVector 0.  0.  4. mm
#AIR_HOLE2 2 mm
/gate/Phantom1/daughters/name AIR_hole2
/gate/Phantom1/daughters/insert box
/gate/AIR_hole2/geometry/setXLength  19.2 cm
/gate/AIR_hole2/geometry/setYLength  0.4 mm
/gate/AIR_hole2/geometry/setZLength   2 mm
/gate/AIR_hole2/placement/setTranslation -10.45  0.38 -13.5 cm
/gate/AIR_hole2/setMaterial Air
/gate/AIR_hole2/vis/forceSolid
/gate/AIR_hole2/vis/setColor green
/gate/AIR_hole2/vis/setVisible 1
/gate/AIR_hole2/attachPhantomSD
/gate/AIR_hole2/repeaters/insert linear
/gate/AIR_hole2/linear/setRepeatNumber 66
/gate/AIR_hole2/linear/setRepeatVector 0.  0.  4. Mm
```

```
# BAR3 3 mm
/gate/Phantom1/daughters/name bar3
/gate/Phantom1/daughters/insert box
/gate/bar3/geometry/setXLength  19.2 cm
/gate/bar3/geometry/setYLength  3.25 mm
/gate/bar3/geometry/setZLength  3.00 mm
/gate/bar3/placement/setTranslation 10.45  0.38  13.85 cm
/gate/bar3/setMaterial Lead
/gate/bar3/repeaters/insert linear
/gate/bar3/linear/setRepeatNumber 44
/gate/bar3/linear/setRepeatVector 0.  0.  6.0 mm
#AIR_HOLE3 3 mm
/gate/Phantom1/daughters/name AIR_hole3
/gate/Phantom1/daughters/insert box
/gate/AIR_hole3/geometry/setXLength  19.2 cm
/gate/AIR_hole3/geometry/setYLength  0.4 mm
/gate/AIR_hole3/geometry/setZLength  3.00 mm
/gate/AIR_hole3/placement/setTranslation 10.45  0.38  13.85 cm
/gate/AIR_hole3/setMaterial Air
/gate/AIR_hole3/repeaters/insert linear
/gate/AIR_hole3/linear/setRepeatNumber 44
/gate/AIR_hole3/linear/setRepeatVector 0.  0.  6.0 mm
#BAR4 3.5 mm
/gate/Phantom1/daughters/name bar4
/gate/Phantom1/daughters/insert box
/gate/bar4/geometry/setXLength  3.5 mm
/gate/bar4/geometry/setYLength  3.25 mm
/gate/bar4/geometry/setZLength  26.2 cm
/gate/bar4/placement/setTranslation   -10.45  0.1975  13.85 cm
/gate/bar4/setMaterial Lead
/gate/bar4/repeaters/insert linear
/gate/bar4/linear/setRepeatNumber 28
/gate/bar4/linear/setRepeatVector 7.0  0.  0. Mm
#AIR_HOLE4 3.5 mm
/gate/Phantom1/daughters/name AIR_hole4
/gate/Phantom1/daughters/insert box
/gate/AIR_hole4/geometry/setXLength  3.5 mm
/gate/AIR_hole4/geometry/setYLength  0.4 mm
/gate/AIR_hole4/geometry/setZLength  26.2 cm
/gate/AIR_hole4/placement/setTranslation   -10.45  0.38  13.85 cm
/gate/AIR_hole4/setMaterial Air
/gate/AIR_hole4/repeaters/insert linear
/gate/AIR_hole4/linear/setRepeatNumber 28
/gate/AIR_hole4/linear/setRepeatVector 7.0  0.  0. mm
```

Appendix 4

Shielding

```
/gate/world/daughters/name shielding
/gate/world/daughters/insert box
/gate/shielding/geometry/setXLength 47.0 cm
/gate/shielding/geometry/setYLength 25 mm
/gate/shielding/geometry/setZLength 12. cm
/gate/shielding/placement/setTranslation  0. 2.15  0.  m
/gate/shielding/setMaterial Lead
#HOLE1
/gate/shielding/daughters/name hole1
/gate/shielding/daughters/insert box
/gate/hole1/geometry/setXLength 1 mm
/gate/hole1/geometry/setYLength 20 mm
/gate/hole1/geometry/setZLength 1 mm
/gate/hole1/vis/forceSolid
/gate/hole1/placement/setTranslation  0. -5.  0. mm
HOLE2
/gate/shielding/daughters/name hole2
/gate/shielding/daughters/insert box
/gate/hole2/geometry/setXLength 1 mm
/gate/hole2/geometry/setYLength 20 mm
/gate/hole2/geometry/setZLength 1 mm
/gate/hole2/vis/forceSolid
/gate/hole2/placement/setTranslation  82.5 -5.  0. mm
HOLE3
/gate/shielding/daughters/name hole3
/gate/shielding/daughters/insert box
/gate/hole3/geometry/setXLength 1 mm
/gate/hole3/geometry/setYLength 20 mm
/gate/hole3/geometry/setZLength 1 mm
/gate/hole3/vis/forceSolid
/gate/hole3/placement/setTranslation  165  -5.  0. mm
HOLE4
/gate/shielding/daughters/name hole4
/gate/shielding/daughters/insert box
/gate/hole4/geometry/setXLength 1 mm
/gate/hole4/geometry/setYLength 20 mm
/gate/hole4/geometry/setZLength 1 mm
/gate/hole4/vis/forceSolid
/gate/hole4/placement/setTranslation  -165 -5.  0. mm
HOLE5
/gate/shielding/daughters/name hole5
/gate/shielding/daughters/insert box
/gate/hole5/geometry/setXLength 1 mm
/gate/hole5/geometry/setYLength 20 mm
/gate/hole5/geometry/setZLength 1 mm
/gate/hole5/vis/forceSolid
/gate/hole5/placement/setTranslation  -82.5 -5.  0. mm

/gate/world/daughters/name Phantom1
/gate/world/daughters/insert box
/gate/Phantom1/geometry/setXLength  47.0 cm
/gate/Phantom1/geometry/setYLength  55 mm
/gate/Phantom1/geometry/setZLength  59.5 cm
/gate/Phantom1/placement/setTranslation 0. 0. 0. cm
/gate/Phantom1/setMaterial Lead
```

```
#BAR1 2.5 mm
/gate/Phantom1/daughters/name bar1
/gate/Phantom1/daughters/insert box
/gate/bar1/geometry/setXLength  2.5 mm
/gate/bar1/geometry/setYLength  55 mm
/gate/bar1/geometry/setZLength  26.2 cm
/gate/bar1/setMaterial Air
/gate/bar1/placement/setTranslation  8.25  0. 0. cm
#BAR2 2 mm
/gate/Phantom1/daughters/name bar2
/gate/Phantom1/daughters/insert box
/gate/bar2/geometry/setXLength  2 mm
/gate/bar2/geometry/setYLength  55 mm
/gate/bar2/geometry/setZLength   26.2 cm
/gate/bar2/setMaterial Air
/gate/bar2/placement/setTranslation    -8.25  0.  0. cm
/gate/bar2/repeaters/insert linear
/gate/bar2/linear/setRepeatNumber 1
/gate/bar2/linear/setRepeatVector 0.  0.  4. mm
# BAR3 3 mm
/gate/Phantom1/daughters/name bar3
/gate/Phantom1/daughters/insert box
/gate/bar3/geometry/setXLength  3 mm
/gate/bar3/geometry/setYLength  55 mm
/gate/bar3/geometry/setZLength  26.2 cm
/gate/bar3/setMaterial Air
/gate/bar3/placement/setTranslation   16.5  0.  0. cm
/gate/bar3/repeaters/insert linear
/gate/bar3/linear/setRepeatNumber 1
/gate/bar3/linear/setRepeatVector 0.  0.  6.02 mm
#BAR4 3.5 mm
/gate/Phantom1/daughters/name bar4
/gate/Phantom1/daughters/insert box
/gate/bar4/geometry/setXLength  3.5 mm
/gate/bar4/geometry/setYLength  55 mm
/gate/bar4/geometry/setZLength  26.2 cm
/gate/bar4/setMaterial Air
/gate/bar4/placement/setTranslation    -16.5  0.  0. cm
/gate/bar4/repeaters/insert linear
/gate/bar4/linear/setRepeatNumber 1
/gate/bar4/linear/setRepeatVector 6.98  0.  0. mm
#BAR5 1.5 mm
/gate/Phantom1/daughters/name bar5
/gate/Phantom1/daughters/insert box
/gate/bar5/geometry/setXLength  1.5 mm
/gate/bar5/geometry/setYLength  55 mm
/gate/bar5/geometry/setZLength  26.2 cm
/gate/bar5/setMaterial Air
/gate/bar5/placement/setTranslation    0.  0.  0. cm
```

RESUME

Anes Hayder completed his primary, secondary, and high school education in Mosul, Iraq. He earned a master's degree in Physics from the University of Kufa, Faculty of Science, in 2015. In 2019, Anes Hayder embarked on his doctoral studies in Physics at Karadeniz Technical University in Trabzon, Turkiye.

Articles Published in SCI-Expanded Journals Derived from the Dissertation

Hayder, A., Bayram, T., Gedik, S., Sönmez, B., Duman, P., & Yavruoğlu, C. (2025). Intrinsic performance parameters assessment of various scintillation crystals for a SPECT gamma camera. Nuclear Instruments and Methods in Physics Research Section A: Accelerators, Spectrometers, Detectors and Associated Equipment, 1076, 170447.

Hayder, A., Bayram, T., Gedik, S., Sönmez, B., Duman, P., & Yavruoğlu, C. (2025). Evaluation of Extrinsic Performance Parameters of SPECT Instrument for Various Collimators: Experimental and Monte Carlo Optimization Study. Physica Medica (Submitted).

Conference Proceedings Derived from the Dissertation

Hayder, A., Bayram, T., & Şentürk, Ş., (2023). The Collimator Optimization for ^{133}Xe and ^{201}Tl Isotopes on the Simulation SPECT Imaging Model. 6th Pak – Türk International Conference on Emerging Technologies in the field of Sciences and Engineering (pp.160-165). Karabük, Türkiye.

Other Articles Published in SCI-Expanded Journals

Aynur, H. U., Bayram, T., Hayder, A., & Gedik, S. (2024). Investigation of the effect of crystal dead layer on system performance in Single Photon Emission Computed Tomography: A Monte Carlo simulation study. Radiation Measurements, 107363.

Nabi, J. U., Bayram, T., Böyükata, M., Ullah, A., Hayder, A., & Naqvi, S. Z. (2024). Re-examination of nuclear structure properties and shape co-existence of nuclei around A~70. Nuclear Physics A, 1052, 122941.

Nabi, J. U., Bayram, T., Riaz, M., Ullah, A., Hayder, A., Şenturk, Ş., & Böyükata, M. (2023). Re-examination of β-decay in Hg, Pb and Po Isotopes. Physica Scripta, 98(8), 085314.

Şentürk, Ş., Bayram, T., & Hayder, A. (2024). Production Cross-section and Reaction Yield of ^{76}Br for Nat Se (p, xn)^{76}Br Reaction Channels. Iranian Journal of Science, 1-9.

Bayram, T., Hayder, A., & Şentürk, Ş. (2023). Decay Modes and Half-Life of $^{265-282}$Ds Isotopes. Iranian Journal of Science, 47(3), 969-977.

Bayram, T., & Hayder, A. (2022). An Investigation on Decay Modes and Half-Life of Nobelium Isotopes. Physics of Atomic Nuclei, 85(3), 275-281.

Yousif, S. A. R., Abojassim, A. A., & Hayder, A. (2019). Mapping of natural radioactivity in soil samples of Badra oil field project using GIS program. Ядерна фізика та енергетика, 20(1), 60-69.